
Master's thesis
Computational Physics

# STEM image simulation of radiation damage in tungsten

Aslak Fellman

06.05.2021

Supervisor(s): Andrea Sand

Examiner(s): Kai Nordlund
Andrea Sand

University of Helsinki
Faculty of Science

P.O. 64 (Gustaf Hällströms gata 2a)
00014 University of Helsinki

HELSINGIN YLIOPISTO — HELSINGFORS UNIVERSITET — UNIVERSITY OF HELSINKI

| Tiedekunta — Fakultet — Faculty | Laitos — Avdelning — Department |
|---|---|
| Faculty of Science | Department of Physics |

Tekijä — Författare — Author

Aslak Fellman

Työn nimi — Arbetets titel — Title

STEM image simulation of radiation damage in tungsten

| Työn laji — Arbetets art — Level | Aika — Datum — Month and year | Sivumäärä — Sidantal — Number of pages |
|---|---|---|
| Master's thesis | 06.05.2021 | 56 |

Tiivistelmä — Referat — Abstract

The plasma-facing materials of future fusion reactors are exposed to high doses of radiation. The characterization of the radiation damage is an essential part in the study of fusion relevant materials. Electron microscopy is one of the most important tools used for characterization of radiation damage, as it provides direct observations of the microstructure of materials. However, the characterization of defects from electron microscope images remains difficult. Simulated images can be used to bridge the gap between experimental results and models.

In this thesis, scanning transmission electron microscope (STEM) images of radiation damage were simulated. Molecular dynamics simulations were employed in order to create defects in tungsten. STEM images were simulated based on the created systems using the multislice method. A database of images of $\langle 001 \rangle$ dislocation loops and defects produced from collision cascade simulations was generated. The simulated images provide insight into the observed contrast of the defect structures. Differences in the image contrast between vacancy and interstitial $\langle 001 \rangle$ dislocation loops were reported. In addition to this, the results were compared against experimental images and used in identification of a dislocation loop. The simulated images demonstrate that it is feasible to simulate STEM images of radiation damage produced from collision cascade simulations.

Avainsanat — Nyckelord — Keywords

Tungsten, Radiation damage, Molecular dynamics, STEM, Electron microscopy, Multislice method

Säilytyspaikka — Förvaringsställe — Where deposited

Kumpula Science Library

Muita tietoja — Övriga uppgifter — Additional information

HELSINGIN YLIOPISTO — HELSINGFORS UNIVERSITET — UNIVERSITY OF HELSINKI

| Tiedekunta — Fakultet — Faculty | Laitos — Avdelning — Department |
|---|---|
| Matematisk-naturvetenskapliga fakulteten | Avdelningen för fysik |

Tekijä — Författare — Author

Aslak Fellman

Työn nimi — Arbetets titel — Title

STEM image simulation of radiation damage in tungsten

| Työn laji — Arbetets art — Level | Aika — Datum — Month and year | Sivumäärä — Sidantal — Number of pages |
|---|---|---|
| Magistersavhandling | 06.05.2021 | 56 |

Tiivistelmä — Referat — Abstract

Plasmariktade material i framtida fusionsreaktorer är utsatta för höga strålningsdoser. Karakterisering av strålningsskador är en grundläggande del i forskningen av fusions relevanta material. Elektronmikroskopi är ett av de viktigaste verktyg som används i karakterisering av strålningsskador, på grund av att metoden ger direkta observationer om materialets mikrostruktur. Trots detta är karakteriseringen av defekter från elektronmikroskop bilder utmanande. Simulerade bilder kan användas för att sammankoppla experimentella resultat med modeller.

I denna avhandling simulerades transmissions svepelektronmikroskop (STEM) bilder av strålningsskador. Molekyldynamiska simuleringar användes för att skapa strålningsskador i volfram. STEM bilder skapades på basis av dessa system, med hjälp av månglager metoden. En databas genererades med bilder av $\langle 001 \rangle$ dislokationsslingor och defekter genererade från simuleringar av kollisionskaskader. Resultaten ger oss insikt i den observerade kontrasten av defekterna. Skillnader mellan vakans och interstitial $\langle 001 \rangle$ dislokationer rapporterades. Utöver detta, jämfördes resultaten med experimentella bilder och användes för att identifierar en dislokationsslinga. De simulerade bilderna demonstrerar att det är framkomligt att skapa simulerade STEM bilder av strålningsskador producerade med kollisionskaskadsimuleringar.

Avainsanat — Nyckelord — Keywords

Volfram, Strålningsskador, Molekyldynamik, STEM, Elektronmikroskopi, Månglager metod

Säilytyspaikka — Förvaringsställe — Where deposited

Vetenskapsbiblioteket i Gumtäkt

Muita tietoja — Övriga uppgifter — Additional information

HELSINGIN YLIOPISTO — HELSINGFORS UNIVERSITET — UNIVERSITY OF HELSINKI

| Tiedekunta — Fakultet — Faculty | Laitos — Avdelning — Department |
|---|---|
| Matemaattis-luonnontieteellinen tiedekunta | Fysiikan osasto |

Tekijä — Författare — Author

Aslak Fellman

Työn nimi — Arbetets titel — Title

STEM image simulation of radiation damage in tungsten

| Työn laji — Arbetets art — Level | Aika — Datum — Month and year | Sivumäärä — Sidantal — Number of pages |
|---|---|---|
| Maisterin tutkinto | 06.05.2021 | 56 |

Tiivistelmä — Referat — Abstract

Fuusioreaktoreiden plasmavastaiset materiaalit altistuvat korkeille säteilyannoksille. Säteilyvaurioiden karakterisointi on oleellinen osa fuusiorelevanttien materiaalien tutkimusta. Elektronimikroskopia on yksi tärkeimmistä menetelmistä joita käytetään säteilyvaurioiden karakterisointiin, sillä se mahdollistaa materiaalin mikrostruktuurin kuvantamisen. Kuitenkin vaurioiden karakterisointi elektronimikroskooppikuvista on haasteellista. Simulaatioiden avulla voidaan paremmin yhdistää kokeelliset tulokset malleihin.

Tässä tutkielmassa simuloitiin pyyhkäisy-läpivalaisuelektronimikroskooppi (STEM) kuvia säteilyvaurioista. Säteilyvaurioita luotiin volframiin hyödyntäen molekyylidynamiikka simulaatioita. STEM kuvia simuloitiin luotujen systeemien pohjalta, hyödyntäen moniviipale menetelmää. STEM kuvista luotiin tietokanta. Simuloidut kuvat antavat viitteitä säteilyvaurioiden muodostamasta kontrastista. Interstitiaali ja vakanssi dislokaatioiden välillä havaittiin eroavaikuusia kuvien kontrastissa. Tämän lisäksi simuloituja kuvia vertailtiin kokellisiin tuloksiin ja niiden avulla pystyttiin tunnistamaan dislokaatio. Simulaatiot osoittivat, että törmäyskaskadisimulaatioista tuotettujen säteilyvaurioiden STEM simulointi on toteutettavissa.

Avainsanat — Nyckelord — Keywords

Volframi, Säteilyvaurio, Molekyylidynamiikka, STEM, Elektronimikroskopia, Moniviipale menetelmä

Säilytyspaikka — Förvaringsställe — Where deposited

Kumpulan tiedekirjasto

Muita tietoja — Övriga uppgifter — Additional information

# Contents

# 1. Introduction

Radiation damage causes changes to the mechanical properties of materials [1]. In applications where materials are exposed to high doses of radiation, the understanding of damage mechanisms is of consequential importance. Prolonged exposure to high radiation doses causes changes such as swelling and void formation [2, 3]. These effects can have fatal consequences on the structural integrity of the material. Due to this, there is a significant amount of research interest into radiation damage in plasma facing materials used in future fusion reactors [4, 5]. Tungsten is one of the main candidates for the use in such components [6].

The characterization of defects is an essential part in the study of radiation damage. Electron microscopy has become one of the most important tools for the characterization of defects. It allows for direct observations of the microstructure of a material, providing evidence for different damage mechanisms. However, the characterization of the defects from images produced by electron microscopes remains challenging [7]. Several methods have been developed for the characterization of defects such as dislocations and voids using transmission electron microscopes (TEM) [8]. However, the visibility of smaller defect clusters is a major limitation of TEM [9]. Scanning transmission electron microscopy (STEM) can be used to overcome this limitation [10].

Simulated images are sometimes necessary in order to interpret images obtained from electron microscopes. Studies have been conducted on the characterization of dislocations using simulated TEM images [9, 11]. In these studies several computer generated images are used to determine properties such as size and orientation of dislocations. Recently, dislocations have been studied using diffraction contrast image simulations and comparing these to experimental images [12, 13]. STEM image simulations have also been used to study defects [14, 15]. Furthermore, Phillips *et al.* have investigated diffraction contrast STEM simulations of dislocations [16].

In this thesis, STEM images were simulated of radiation damage in tungsten. Molecular dynamics (MD) simulations were used to create systems containing various types of defects. STEM images were simulated based on the created systems. The theory behind the methods for both the simulation of radiation damage and STEM images is presented. The observed contrast caused by the defects is presented and discussed.

# 2. Radiation damage in tungsten

Tungsten is going to be used in structural components such as divertors in future fusion reactors [17]. This is due to its suitable mechanical properties such as its high melting point and ability to resist erosion [18, 19]. However, the longterm changes to the mechanical properties of tungsten, due to extended periods of radiation, is a major concern. Neutron irradiation causes void formation, dislocation loops and swelling in tungsten [2, 20, 21]. The characterization of these defects is of paramount importance for the study of radiation damage accumulation. The extreme environments existing in fusion reactors are experimentally inaccessible, hence a significant amount of effort has been made towards the modeling and simulation of damage processes in these environments [22].

## 2.1 Lattice defects

Materials such as tungsten have a regular crystal structure, which can mathematically be described using a Bravais lattice [23]. This means that each atom in the structure can be defined by a linear combination of basis vectors. Essentially, lattice defects can be thought of as deviations from this ideal structure. The lattice structure of tungsten is the body centered cubic (BCC) structure. Point defects are the simplest form of defects that can be defined in a lattice. Vacancies can be thought of as empty lattice sites which would normally be occupied by an atom. Interstitials on the other hand are atoms which are located between filled lattice sites. Another important defect type is the dislocation. There are two main types of dislocations. Firstly, we have screw dislocations, where a helical path can be traced around the dislocation line. Secondly, we have edge dislocations, where an extra atom plane is either removed or added in between the atomic planes of the lattice. Edge dislocations can form loops where the dislocation line connects back on itself. Dislocation loops are classified by the direction of the normal vector of the dislocated plane. This vector is called the Burgers vector. In figure 2.1 we have the two different types of dislocations present in tungsten. Figure 2.1a shows the $\langle 100 \rangle$ -loop, where the Burgers vector is oriented in the $\langle 100 \rangle$ direction in Miller index notation. Figure 2.1b shows a $\langle 111 \rangle$ -loop, where the whole system is rotated so that we are looking at the lattice from the $\langle 111 \rangle$ direction. Dislocations compress and stretch the lattice, introducing

strain on the neighboring atoms. In addition to this, point defects can congregate together forming defect clusters. Figure 2.1c shows an illustration of a vacancy cluster (void).

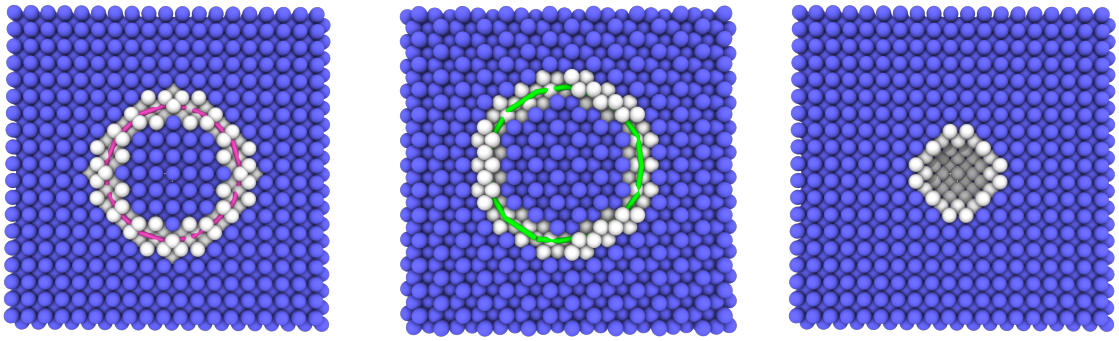

**(a)** ⟨100⟩ loop **(b)** ⟨111⟩ loop **(c)** Vacancy cluster

**Figure 2.1:** Illustration of different vacancy type defects. Blue spheres represent atoms with their local environment identified as BCC, white atoms have no identified lattice structure, magenta line is a dislocation loop oriented in the ⟨100⟩ direction and green line is a dislocation loop oriented in the ⟨111⟩ direction.

Besides the defects described, radiation damage can manifest as more complex defect structures. In this thesis we considered both systematically created defects as well as defect structures produced from simulations of collision cascades.

## 2.2 Collision cascade

The deuterium-tritium reactions in fusion reactors produce $\sim$ 14 MeV neutrons which are not contained by the magnetic field of the reactor [4]. These neutrons can cause high energy recoils resulting in collision cascades. The initial recoil atom is called the primary knock-on atom (PKA). The PKA starts to collide with its surrounding environment, transferring its kinetic energy in the process. Subsequently the neighboring atoms collide with other atoms and so forth, causing a collision cascade. Figure 2.2 shows the typical stages of a collision cascade. Firstly, the PKA initiates the collision cascade, where colliding atoms produce a region with an underdense core and dense fringes [24]. The atoms in this stage are in a disordered state and can essentially be considered being in a liquid phase. This process is usually referred to as a thermal spike or heat spike. After the expansion, the dense outer regions start to recrystallize back into the low density core left behind. During the recrystallization some defects remain in the system. These defects are called primary radiation damage, which will continue to evolve due to thermal effects.

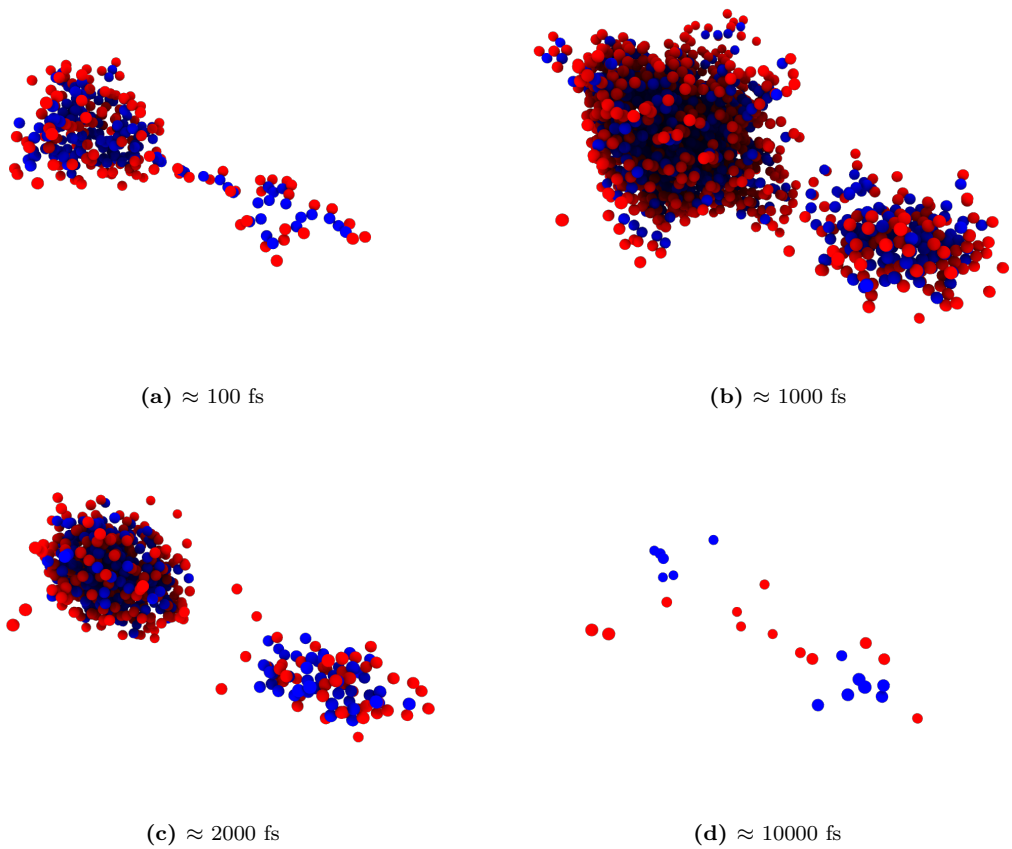

**(a)** ≈ 100 fs **(b)** ≈ 1000 fs

**(c)** ≈ 2000 fs **(d)** ≈ 10000 fs

**Figure 2.2:** Example cascade in pure tungsten with 30 keV PKA-energy, red spheres represent interstitials and blue spheres represent vacancies.

Primary radiation damage has been studied extensively using MD [24]. These MD studies typically have been performed with the perfect crystal as the initial state. In real world applications with high radiation doses, such as in future fusion power plants, there is a higher probability that a collision cascade occurs in regions with pre-existing defects. The effects of this cascade-defect overlap is an expanding area of research. There are different methods of simulating cascade overlap effects. We can perform multiple cascades on the same region and look at the resulting damage from consecutive cascades [25, 26]. Alternatively, we can produce simulations where predetermined defects are created and then cascades are performed on these systems [27, 28]. In this thesis we employ cascade-overlap simulations of the latter kind, with a focus on vacancy type defects.

# 3. Molecular dynamics simulation of radiation damage

## 3.1 Molecular dynamics

Molecular dynamics (MD) is a simulation method that involves solving the equations of motion for atomistic systems. MD was developed in 1957 and was initially used to simulate vibrating molecules [29]. The basic structure of a MD algorithm is as follows:

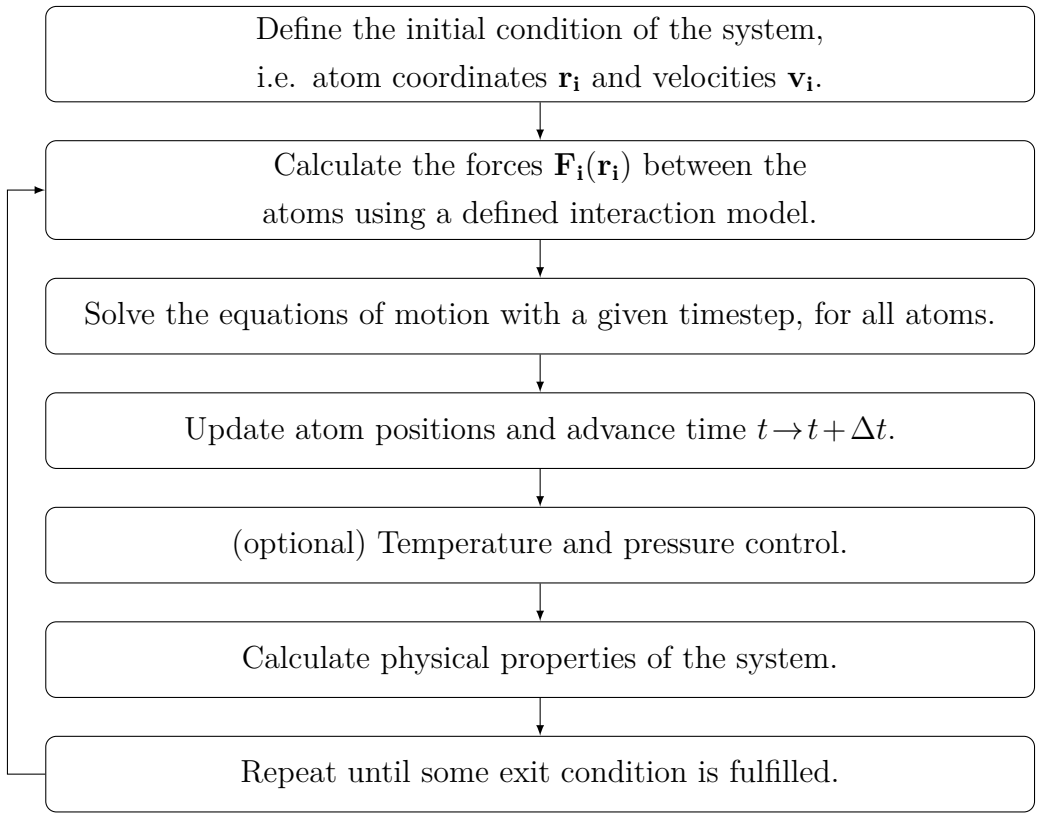


The initial condition of the simulation is defined by the atom positions $\mathbf{r_i}$ and the velocities $\mathbf{v_i}$, which can be set to correspond to the temperature distribution of the system. There are significant physical differences between surfaces and bulk materials [30]. In order to simulate bulk properties a very large number of atoms is required. In practice this is

achieved by the use of periodic boundary conditions (PBC), where an atom crossing the border of the simulation cell is then transferred to the opposite side.

The familiar Newton's equations of motion are presented in equation 3.1, where $m_i$ and $a_i$ are the mass and acceleration of the $i$th atom . Using the interatomic potential $V$, the forces $\mathbf{F_i}(\mathbf{r_i})$ can be calculated.

$$\mathbf{F_i}(\mathbf{r_i}) = m_i \mathbf{a_i} = -\nabla_{r_i} V(\mathbf{r_i}) \tag{3.1}$$

There are multiple different approaches to numerically solving the equations of motion of a given system. Common methods include velocity verlet, leap frog and predictor-corrector methods such as Gear5 [31]. The trade-off between these methods comes down to computational efficiency and the accuracy of the calculation. All of these methods rely on knowing the acceleration of each individual atom, which in turn is solved from the equations of motion. As a consequence, the interatomic potential becomes paramount for the accuracy of MD.

## 3.2 Interatomic potentials

Ideally, the interatomic forces would be calculated from quantum mechanical models, but these become very quickly computationally cumbersome. To create an efficient MD model the potential needs to be simultaneously as simple as possible while not compromising the physical accuracy of the effects that it is used to describe.

A common model for describing metals is the so called embedded-atom method (EAM). EAM models describe positive ionic cores that are bound to the local negative electron density in addition to a simple pair-potential [32]. The potential energy of the EAM model is described in equation 3.2, where $V_i$ is the pair-potential and $G_i$ is the embedding energy that is a function of the electron density $\rho$.

$$E = \sum_i G_i \left( \sum_{i \neq j} \rho_j(r_{ij}) \right) + \frac{1}{2} \sum_{i \neq j} V(r_{ij}) \tag{3.2}$$

The embedding function $G$ can have different expressions and these are generally fitted to data obtained using quantum mechanical methods such as density functional theory. Short-range interactions can be implemented in the pair-potential with a screened Coulomb potential. Equation 3.3 shows the commonly used Ziegler-Biersack-Littmark (ZBL) potential [33].

$$\begin{aligned} V(r) &= \frac{e^2}{4\pi\epsilon_0} \frac{Z_1 Z_2}{r} \phi(r/a) \\ a &= \frac{0.8854 a_0}{Z_1^{0.23} + Z_2^{0.23}} \end{aligned} \tag{3.3}$$

Here, $Z_1$ and $Z_2$ represent the atomic numbers, $a_0$ is the Bohr radius and $\phi$ is the fitted universal screening function shown in equation 3.4.

$$\phi(x) = 0.1818e^{-3.2x} + 0.5099e^{-0.9423x} + 0.2802e^{-0.4029x} + 0.02817e^{-0.2106x} \tag{3.4}$$

EAM potentials don't take into account directional bonding, limiting their use for materials with covalent bonds. In these cases bonding order potentials such as the Tersoff potential are more suitable [34].

## 3.3 Timestep

A collision cascade is a highly non-equilibrium process. Initially, energies in the system are very high, meaning that a small timestep is needed to uphold conservation of energy. The very small timestep is essential in the early phases of the cascade, whereas a larger timestep would be sufficient for the later stages. Simulating the whole collision cascade process with a timestep required for the early stage is very resource intensive. An adaptive timestep can be implemented to overcome this limitation. This means that the timestep is scaled according to system properties. The simulation code *PARCAS* [35] used for the radiation damage simulations in this thesis, uses an adaptive timestep given in equation 3.5

$$\Delta t_{\text{new}} = \min\left(\frac{k_t}{v_{\max}}, \frac{E_t}{F v_{\max}}, 1.1\Delta t_{\text{old}}, \Delta t_{\text{equi}}\right) \tag{3.5}$$

where the timestep is determined by proportionality constants $k_t$ and $E_t$ in addition to the maximum velocity and force $F$ in the system. The timestep is also limited so it can't increase more than 10 % at a time.

## 3.4 Electronic stopping

At higher energies, electronic effects become relevant and have to be taken into account when modeling collision cascades. The energy loss of an ion per unit length traveled can be defined by a quantity called stopping power [33]. In the case of ion irradiation, stopping power can be described consisting of three parts.

$$S = -\frac{dE}{dx} = S_e + S_n + S_{\text{reactions}} \tag{3.6}$$

Electronic stopping $S_e$ can be described as a friction force between the projectile and the electrons in the material. $S_n$ represents the nuclear stopping that is the energy loss experienced by the collisions between atoms and the projectile. Additionally, there can be stopping caused by nuclear reactions which become relevant at very high energies. The effects of electronic stopping become relevant to cascade simulations due to the high

energy of the recoiling atoms. In *PARCAS*, the electronic stopping experienced by the atoms is taken into account as a friction force represented in equation 3.7, where the values used for $S_e$ have been tabulated from *SRIM* calculations [36].

$$\Delta v = \Delta t \frac{S_e}{m} \tag{3.7}$$

## 3.5 Temperature and pressure control

Collision cascades introduce a significant amount of energy to the simulated system. In order to model the thermal diffusion of the cascade region into the surrounding material, temperature control can be applied for the border atoms of the simulation. This is usually modeled by introducing a coupling with an external heat-bath. One method of temperature control is the Berendsen method [37], where the velocities are scaled by a factor $\lambda$ given in equation 3.8. $T_0$ represents the target temperature, $\Delta t$ is the timestep and $\tau_T$ is a coupling constant which determines the strength of the coupling.

$$\lambda = \sqrt{1 - \frac{\Delta t}{\tau_T}(\frac{T_0}{T} - 1)} \tag{3.8}$$

Pressure control can be applied in order to avoid the pressure wave produced by the cascade from self-interacting over the periodic boundaries. Similarly as in the case of temperature control we can use a scaling factor $\mu$ that scales the simulation cell size according to the following equation.

$$\mu = \sqrt[3]{1 + \frac{\Delta t}{\tau_P}\beta[P - P_0]} \tag{3.9}$$

In addition to the coupling factor $\tau_P$ we also have the isothermal compressibility of the system $\beta$. The Berendsen method is a quite naive scaling method and is by no means suitable for all applications. There are multiple different approaches to temperature and pressure control. A couple notable examples are the Nosé-Hoover method [38], Andersen method [39] and Parrinello-Rahman method [40].

# 4. Electron microscope image simulation

## 4.1 The electron microscope

In the 1920s, the French physicist Luois de Broglie proposed that particles of matter can exhibit wave-like properties [41]. The wavelength of these "matter waves" in the case of accelerated electrons was estimated to be five orders of magnitude shorter than light waves [42], which in turn allows the electron microscope to have superior resolution compared to conventional light microscopes. The first electron microscopes were developed in the early 1930s [43, 42]. Conventional transmission electron microscopes (CTEM) work on the basis of accelerated electrons that penetrate a specimen, after which the transmitted electron beam is focused using magnetic lenses, forming an image. Shortly after the development of CTEM, the scanning transmission electron microscope (STEM) was invented [44]. STEM works similarly to CTEM, but for STEM the accelerated electrons are focused before the specimen. The focused electron beam is scanned across the surface of the specimen, forming the image pixel by pixel. In practice, there are always going to be some distortions in the final image that do not represent the real structure of the specimen. Deviations from the ideal image are called aberrations. Aberrations are one of the major limiting factors on the resolution of an electron microscope. This is why aberration correction is in itself a significant field of research in electron microscopy [45]. Figure 4.1 shows a simplified schematic of an aberration corrected scanning transmission electron microscope. At the top of the illustration we have the electron gun, which produces the electron beam. The electrons are accelerated to the target energy and in some cases passed through a monochromator. The monochromator filters the electron beam's energy distribution. This narrows the energy spread of the electron beam, improving resolution. The electron beam is then condensed by the condenser lens and passed through the aberration corrector. The objective lens focuses the beam on the specimen, forming a probe with a given convergence angle (probe semi-angle). Scanning coils move the focused probe across the specimen in a raster fashion. The beam passes through the specimen, scattering and

interacting in the process. The outcoming beam is then measured using detectors. A bright-field (BF) detector can be used to measure the intensity of the electron beam that is on the optical axis of the microscope. Annular dark-field (ADF) detectors can be used to measure the intensity of scattered electrons. The variation in the measured intensities between different probe positions provides the contrast of the image.

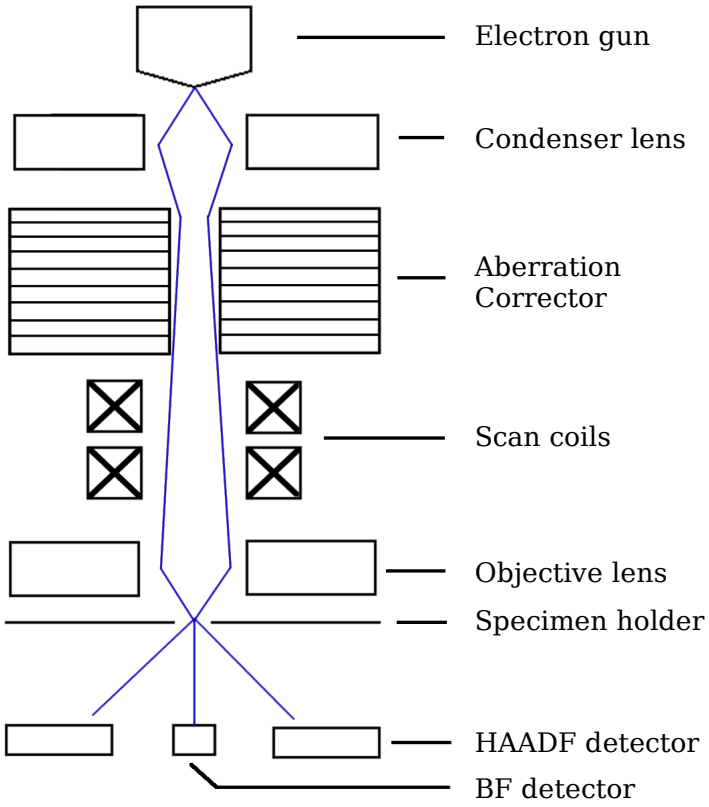


**Figure 4.1:** Simplified schematic of a scanning transmission electron microscope with an aberration corrector.

The purpose of aberration correction is to identify the aberrations present in the system and mitigate their effects. In practice this is done by using magnetic lenses that produce new aberrations that counter the aberrations previously present. Aberrations can be mathematically represented using an aberration function [46]. The theoretical resolution of an electron microscope is mainly limited by the spherical aberrations of the system [47].

## 4.2 STEM image simulation

On a fundamental level, STEM image simulation reduces to the modeling of the scattering of fast moving electrons in a material. Ideally this could be achieved by solving the Schrödinger equation for a fast moving electron. However, the electrons in STEM can be accelerated to several hundreds of keVs, meaning that relativistic effects have to be taken into account. In theory, the Dirac equation provides a framework for solving relativistic wave equations, but is considerably more computationally cumbersome. The models used in STEM simulations therefore use the Schrödinger equation with relativistic corrections to the mass and wavelength of the electrons [46].

There are multiple different approaches to solving the Schrödinger equation for a fast moving electron. One approach is to use the so called Bloch wave method, where the electron wave function is represented by Bloch waves which have built in the periodicity of the lattice. Using this Bloch wave representation one can solve the Schrödinger equation, by reducing the equation to an eigenvalue problem. A more detailed description of this method can be found in [46]. This method assumes a periodic lattice and might therefore not be suitable for simulation of defects. The multislice method is another method that can be used to simulate STEM images. This method is computationally more efficient, which makes it more suitable for larger simulations. The simulations performed for this thesis are based on the multislice method.

## 4.3 Multislice method

The multislice method was first devised by Cowley and Moodie in 1957 [48]. Figure 4.2 shows the main idea of the method, where the specimen is divided into thin slices. For each slice a projected potential is calculated. The wave function is then iteratively transmitted through the potential and propagated to the next slice. The projected potential is calculated by integrating the atomic potential along the optical axis of the specimen for each slice. It must be noted that the atomic potential used for the calculation is distinct from the interatomic potential discussed in section 3.2. The atomic potential can be parametrized from electron scattering factors produced from relativistic Hartree-Fock calculations [46].

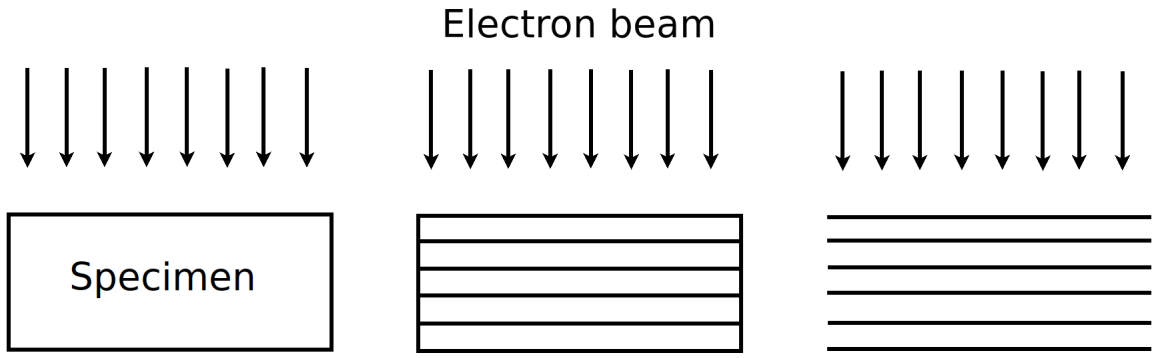


**Figure 4.2:** Illustration of the multislice method.

The mathematical description of the multislice method [46, 49] starts with the wave equation of a fast moving electron.

$$\begin{aligned} \frac{\partial \Psi(x,y,z)}{\partial z} &= [A+B]\Psi(x,y,z) \\ A &= \frac{i\lambda}{4\pi}\nabla_{xy}^2 \\ B &= i\sigma V(x,y,z) \end{aligned} \tag{4.1}$$

Here, $A$ and $B$ are noncommuting operators and $\Psi$ is the electron wave function. $\lambda$ is the wavelength of the incident electron and $\sigma$ is an interaction parameter $\sigma = \frac{2\pi m e \lambda}{h^2}$. A solution of equation 4.1 for a thin slice can be found in equation 4.2 where $v_{\Delta z}$ is the projected potential shown in equation 4.3.

$$\Psi(x,y,z+\Delta z) = \exp\left[\frac{i\lambda}{4\pi}\Delta z \nabla_{xy}^2 + i\sigma v_{\Delta z}(x,y,z)\right]\Psi(x,y,z) \tag{4.2}$$

$$v_{\Delta z}(x,y,z) = \int_z^{z+\Delta z} V(x,y,z')dz' \tag{4.3}$$

From this, the general multislice equation can be derived using a lowest order factorization.

$$\Psi(x,y,z+\Delta z) = \exp\left(\frac{i\lambda\Delta z}{4\pi}\nabla_{xy}^2\right)\exp[i\sigma v_{\Delta z}(x,y,z)]\Psi(x,y,z) + \mathcal{O}(\Delta z^2) \tag{4.4}$$

The expression $\exp[i\sigma v_{\Delta z}(x,y,z)]$ can be interpreted as the transmission function $t(x,y,z)$. Similarly the expression $\exp\left(\frac{i\lambda\Delta z}{4\pi}\nabla_{xy}^2\right)$ can be interpreted as the propagator function $p(x,y,\Delta)\otimes$ with a two-dimensional convolution in x and y. Using this, the equation can be rewritten in a cleaner form.

$$\Psi(x,y,z+\Delta z) = p(x,y,\Delta z) \otimes [t(x,y,z)\Psi(x,y,z)] + \mathcal{O}(\Delta z^2) \tag{4.5}$$

The numerical efficiency of the multi-slice equation 4.5, can be further improved by the use of Fourier transforms. Equation 4.6 describes the wave function at the $n$th slice in this form.

$$\Psi_{n+1} = FT^{-1}\{p_n(x, y, \Delta z_n)FT[t_n(x, y, z)\Psi_n(x, y, z)]\} + \mathcal{O}(\Delta z^2) \tag{4.6}$$

There are multiple other considerations when it comes to the simulation of STEM images. A simplified description of the multislice method used to simulate STEM can be defined as follows:

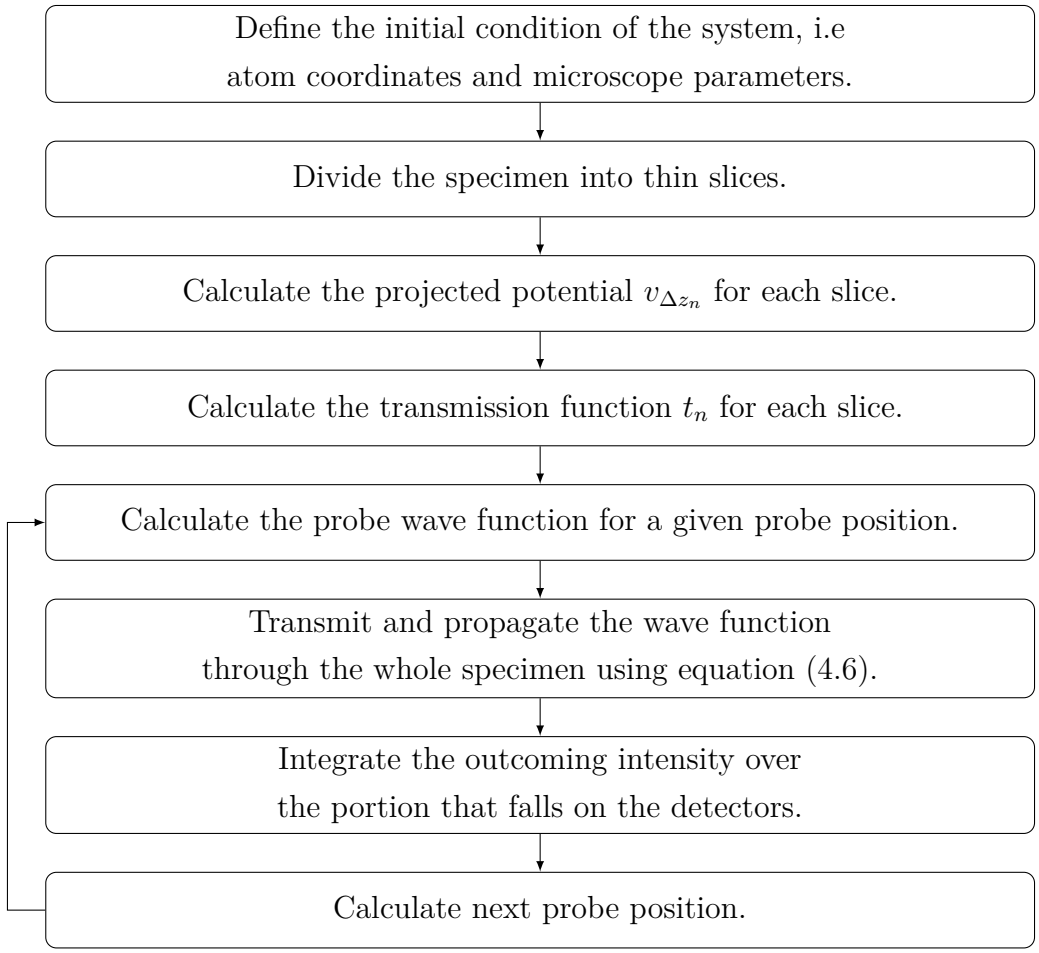


The incident probe at position $\mathbf{x}_p$ can be calculated from

$$\psi(\mathbf{x}, \mathbf{x}_p) = A_p \mathrm{FT}^{-1}\{\exp[-i\chi(\mathbf{k}) + 2\pi i\mathbf{k} \cdot \mathbf{x}_p]A(\mathbf{k})\} \tag{4.7}$$

Where $\mathbf{k}$ represent the reciprocal space coordinates, $\chi$ is the aberration wave function, $A_p$ is a normalization constant and $A(\mathbf{k})$ is the aperture function

$$A = \begin{cases} 1 & \text{if } a \leq a_{\max} \\ 0 & \text{otherwise} \end{cases} \tag{4.8}$$

where the function is zero when the angle is greater than the maximum semi-angle allowed by the aperture.

Thermal diffuse scattering is taken into account by using the so called "frozen phonon" approximation [50]. The basic idea is that the atoms are randomly displaced by the root mean squared (RMS) displacement for a given temperature. Multiple different configurations with random displacements are simulated and the final intensity is calculated as the average intensity from the individual simulations [46].

The simulation code *PRISMATIC* [51, 52] was used for the STEM image simulations in this thesis. *PRISMATIC* includes a multi-GPU implementation of the multislice method for the simulations of STEM images.

# 5. Construction of defects

For this thesis, several different kinds of defects were considered. The primary focus was on $\langle 001 \rangle$ -loops created in different orientations. In addition to this, systems were created with cascade damage produced with MD simulations.

The sample thickness ranged from 20-30 nm, which corresponds to a thin experimental sample. Most of the simulations were done with 20 nm sample thickness due to simulation time constraints. The other dimensions of the simulation cell had to be chosen so that the defect is fully contained inside the simulation cell. Furthermore, there needs to be a sufficiently large buffer-zone at edges. Otherwise wrap around errors might be introduced, causing distortions and artefacts.

## 5.1 $\langle 001 \rangle$ dislocation loops

Initially, large simulation cells with pure tungsten were created. Interstitial and vacancy type dislocation loops were created in the $\langle 001 \rangle$ direction. Vacancy loops were created by removing a plane of atoms with a given radius from the center of the cell. Conversely, interstitial loops were created by the addition of a plane of atoms. These dislocations had a diameter of 3 nm (137 interstitials or vacancies). The large initial simulation cells containing the dislocations were thermalized to 300 K. Thermalization was carried out in *PARCAS* by running a MD simulation during which the temperature and pressure were controlled with a Berendsen thermo- and barostat. The MD code *LAMMPS* [53] was used to perform energy minimization on the thermalized systems. Energy minimization was performed in order to ensure that the atoms are located at their low energy positions. Otherwise the thermal displacements of the thermalization is compounded with the RMS displacements used for the frozen phonon sampling, which might exaggerate the thermal effects. For both simulations the Finnis-Sinclair EAM potential by Ackland *et al.* [54] modified by Zhong *et al.* [55] was used. The thermalized and minimized cells were rotated into different orientations and cut to final size. The simulation cell size chosen was $8 \cdot 8 \cdot 20$ nm. The cut systems were then converted to the *PRISMATIC* format. The different orientations correspond to the different beam directions considered, these are listed in table 5.1.

| Beam direction | ⟨001⟩ | ⟨010⟩ | ⟨011⟩ | ⟨110⟩ | ⟨111⟩ |
|---|---|---|---|---|---|

**Table 5.1:** simulation cell orientations (beam directions) used for ⟨001⟩ -loop simulations.

In figure 5.1, some of the considered systems are illustrated using OVITO [56]. The atoms in the middle are removed for the illustration in order to reveal the orientation of the dislocation loop in the simulation cell.

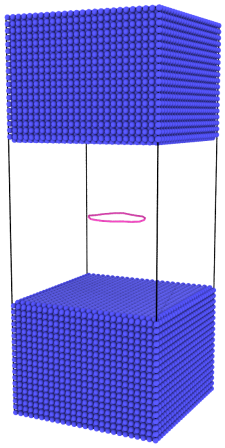

**(a)** Beam direction= ⟨001⟩

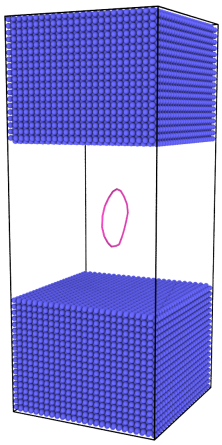

**(b)** Beam direction= ⟨010⟩

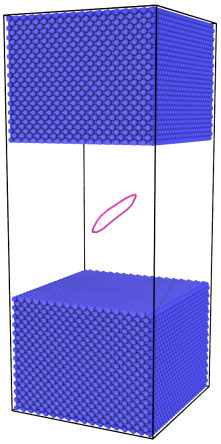

**(c)** Beam direction= ⟨011⟩

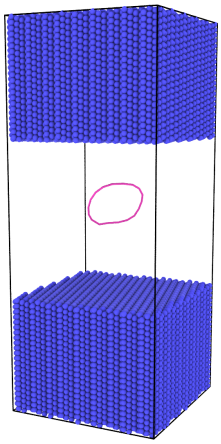

**(d)** Beam direction= ⟨111⟩

**Figure 5.1:** Interstitial ⟨001⟩ -loops in different orientations. Atoms from the middle are made transparent in order to reveal orientation of the dislocation represented by the magenta loop.

## 5.2 Cascade defects

The different cascade damage systems that were created for STEM image simulations are shown in figure 5.2. These systems were chosen from a previous study on the effects of cascade overlap between collision cascades and vacancy type defects [27]. The systems in figure 5.2 are from 30 keV cascade simulations with a pre-existing void containing $N_{\text{vac}} = 259$ vacancies. These simulations were performed by first cutting out a void in the middle of the simulation cell and then thermalizing the system to 300 K. A random atom was chosen a given distance away from the center of the simulation cell. This PKA-atom was given 30 keV kinetic energy towards the center of the cell. A cascade simulation was then initiated and the final configuration was stored after the system had cooled down to approximately the initial temperature of 300 K. The resulting defect structures were analyzed using OVITO's [56] Wigner-Seitz (WS) analysis, where the resulting system is compared to a reference system without defects. The WS analysis works by dividing the system into WS cells. The WS cell defines a region of space that is closer to a specific lattice site than to any other lattice site. An empty site is considered a vacancy, while sites containing more than one atom are classified as interstitial atoms. Dislocation loops and loop segments could be identified from the systems using DXA-analysis [57]. In the cascade overlap study it was reported that dislocation loops can form when a cascade overlaps with a pre-existing vacancy cluster [27]. The systems illustrated in figure 5.2 are all of this type, containing both vacancy clusters and dislocations. In addition to this, the systems contain point defects and smaller clusters (both interstitial and vacancy type). The cascade damaged systems were energy minimized and cut to the cell dimensions of $8 \cdot 8 \cdot 20$ nm.

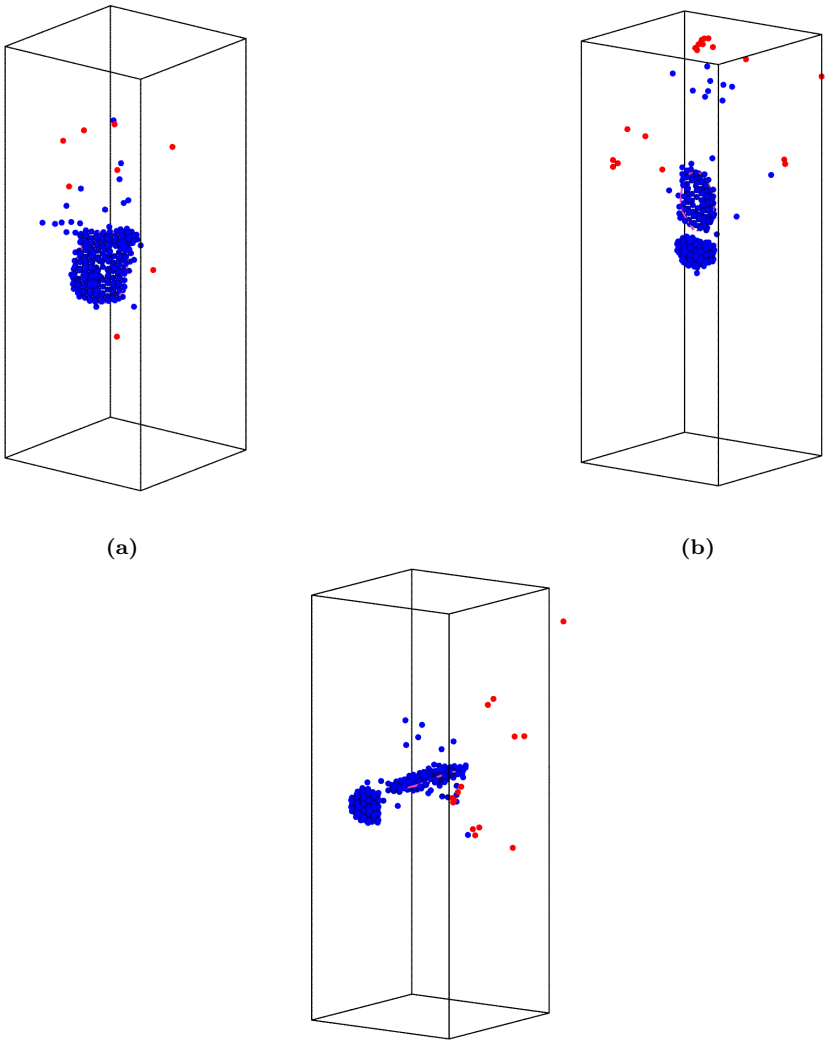

**Figure 5.2:** Cascade damage from 30 keV cascades overlapping with pre-existing voids. Blue spheres represent vacancies, red spheres represent interstitials and magenta lines represent dislocation loops in ⟨100⟩ directions.

A larger defect structure containing multiple different regions with defects was also simulated. The system was chosen from a study by Sand *et al.* [58], where 150 keV cascades were performed in tungsten. At this PKA-energy dislocation loops and more complex defect structures are formed quite frequently. Figure 5.3 shows the system chosen for the STEM simulation. Multiple different sizes and orientations of dislocations are present in the system as well as other defect clusters. Energy minimization was performed on the system. The final systems were cut from the larger minimized simulation cell so that the dimension of the cell was $16 \cdot 16 \cdot 30$ nm. Simulation cells in multiple different orientations were created.

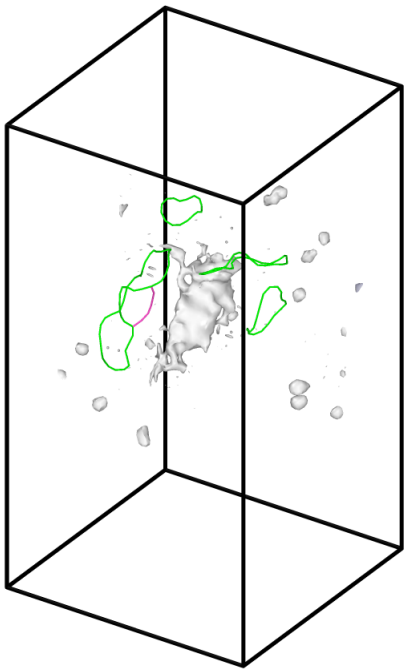

**Figure 5.3:** Cascade damage from a 150 keV cascade in tungsten. White regions illustrate defect structures, green lines represent dislocations in $\langle 111 \rangle$ directions and magenta lines represent dislocations in $\langle 100 \rangle$ directions.

# 6. Simulation methods

## 6.1 Convergence testing and simulation parameters

A significant amount of testing was performed to determine optimal simulation parameters. There were three main considerations when it came to the STEM image simulations. Firstly, there were memory limitations on the specific hardware that the simulations were run on. Secondly, the simulation time was a significant limiting factor. Finally, the fidelity and accuracy of the final data had to be demonstrated. Convergence tests were performed to validate the simulation parameters used. Rather than simulating the whole STEM image, a thin region could be simulated, allowing for multiple simulations to be run quickly. Figure 6.1 shows an example convergence test, where a thin section from the center of a larger system was simulated. This section was chosen so that the defect and pristine crystal is included in it. The intensity profile along a row of pixels (illustrated by the dark line in fig. 6.1) was compared between the different simulation parameters used.

**Figure 6.1:** Example convergence simulation: Interstitial ⟨001⟩ -loop, beam direction ⟨100⟩ , beam energy 100 keV, semi-angle 30 mrad and detector angle 60-80 mrad. The image represents the pixels from a thin slice simulated from the complete system. Atom columns are visible in the image. The darker region to the left is the pristine crystal, while the saturated bright region to the right is where the dislocation is located.

Parameters such as slice thickness and potential bound have an impact on the calculated projected potential. Ideally slice thickness should be as thin as possible, so that a single atom plane is contained within a slice. This is particularly important in samples with defects. The potential bound is a cut-off parameter for the distance up to which the potential is calculated from each atom. It should be sufficiently large so that changes to the final image become negligible. For all simulations the potential bound was set to 2 Å. Figure 6.2 shows the intensity line profiles between runs with different slice thicknesses. In this case we can see that slice thickness 2.6 Å and 2.74 Å seem to diverge from the rest. Slice thickness roughly corresponding to atom plane separation is advisable. Naturally this depends on the crystal orientation and was tested separately for each beam direction.

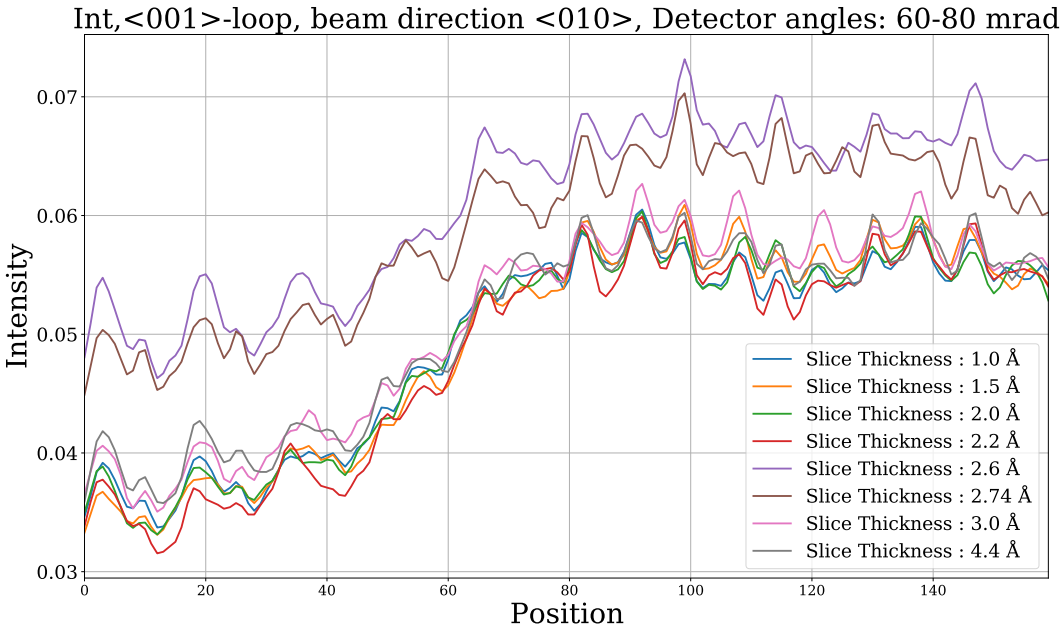


**Figure 6.2:** Interstitial ⟨001⟩ -loop in beam direction ⟨010⟩, 100 keV probe and semi-angle 30 mrad. comparison of intensity between different slice thicknesses. Intensity is in arbitrary units and the position represents the index of the pixel along the line profile.

In addition to slice thickness, the number of frozen phonon configurations used, was tested for all beam directions. The number of frozen phonon configurations determines how accurately the average intensity is calculated when simulating thermal diffuse scattering [50]. However, increasing the number of configurations has a significant computational cost. Figure 6.3 shows the intensity line profile for simulations with different number of frozen phonon configurations. In this case it was determined that 20 frozen phonon configurations was sufficient for a converged intensity. It should be noted that a number that is sufficient for 100 keV and semi-angle 30 mrad might not be adequate for higher energies and semi-angles. The parameters used for the simulations in this thesis are given in table 6.1.

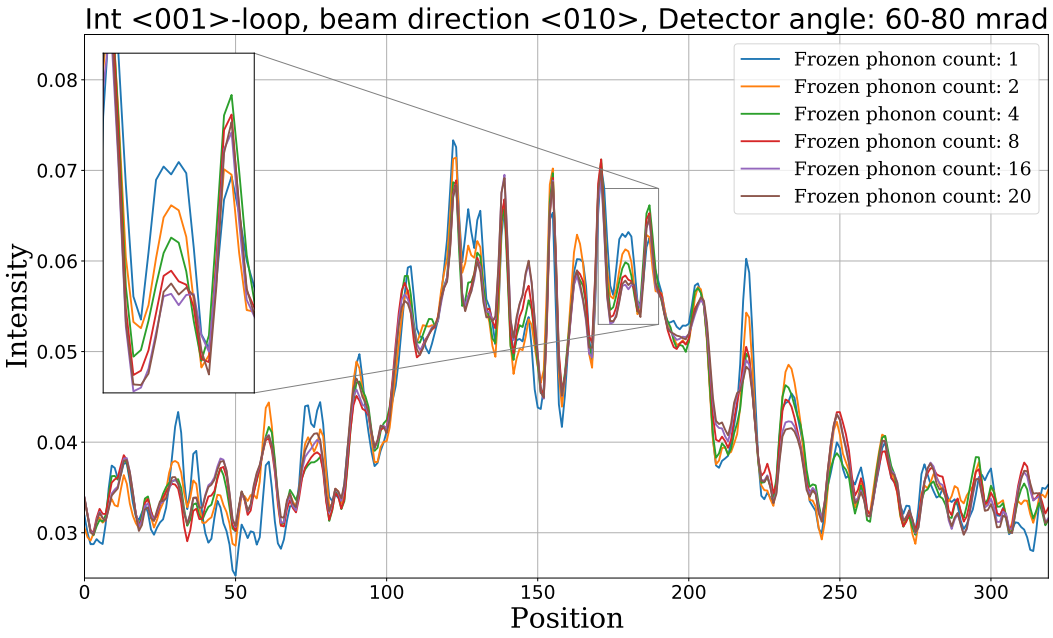


**Figure 6.3:** Interstitial ⟨001⟩ -loop in beam direction ⟨010⟩with 100 keV probe and semi-angle 30 mrad. Comparison of intensities between different number of frozen phonon configurations. Intensity is in arbitrary units and the position represents the index of the pixel along the line profile.

| Energy / Semi-angle | Frozen phonon count | Slice thickness [Å] | probe step [Å] |
|---|---|---|---|
| 100 keV /30 mrad | 20 | $1.5^a$ $2.2^b$ $2.0^c$ | 0.2 |
| 100 keV /35 mrad | 30 | $1.5^a$ $2.2^b$ $2.0^c$ | 0.2 |
| 100 keV /50 mrad | 30 | $1.5^a$ $2.2^b$ $2.0^c$ | 0.2 |
| 100 keV /70 mrad | 50 | $1.5^a$ $2.2^b$ $2.0^c$ | 0.2 |
| 200 keV /70 mrad | 30 | $1.5^a$ $2.2^b$ $2.0^c$ | 0.2 |

[a] Beam direction: ⟨001⟩, ⟨010⟩,
[b] Beam direction: ⟨011⟩, ⟨110⟩
[c] Beam direction: ⟨111⟩

**Table 6.1:** Simulation parameters used for STEM image simulations.

Table 6.1 lists the simulation parameters used for different energies and probe semi-angles. For the 200 keV beam energy the frozen phonon count of 30 was deemed sufficient, while also reducing the computational cost significantly. The probe step determines the real space size of the pixels in the final image. For all simulations this was set to 0.2 Å. The scanning window parameter was set to 0.1-0.9 for both axis. This means that the edges of the simulation cell were not simulated. This was done in order to speed

up the simulation by leaving the buffer region at the edges out of the final image. In *PRISMATIC* the maximum scattering angle $\alpha_{\max}$ is determined by equation 6.1, where $\lambda$ represents the relativistic wavelength of the electron and $p$ is the real space potential grid spacing.

$$\alpha_{\max} = \frac{\lambda}{4p} \tag{6.1}$$

The wavelength $\lambda$ is determined by the beam energy of the probe. For the 100 keV probe, $p$ was set to 0.0881, which corresponds to a maximum scattering angle of slightly above 100 mrad. For the 200 keV probe, $p$ was set to 0.00598, which corresponds to a similar maximum scattering angle. In addition to this, the RMS displacement was set to 0.045491595 Å and the third- and fifth order spherical aberration constants were set to 13.92 $\mu$m and $-13.12$ mm respectively.

## 6.2 STEM simulation methods

For each simulation, several 2-dimensional intensity arrays are stored in the *PRISMATIC* output. These arrays correspond to the integrated intensities for specific detector angles. The detector angles of the final image can be specified after the fact by combining the intensities from a given range of angles. Using the probe defocus we can focus the beam at different depths in the specimen [59]. Series of images with different defocus values were performed for each $\langle 001 \rangle$ system. The defocus values chosen for the series were $0, -50, -75, -100, -125, -150$ and $-200$ Å.

Simulating the large defect structures with the multislice method quickly becomes very computationally expensive and memory intensive. Due to hardware limitations the whole $16 \cdot 16 \cdot 30$ nm large simulation cells could not be simulated in a single run. This limitation was circumvented by running each individual frozen phonon configuration separately and then averaging the intensities from the different runs after the fact. For each individual configuration a new random seed was given, so as to not simulate the same configuration multiple times. This method was tested by running the frozen phonon configurations both separately and in a single run for one of the smaller systems. It was found that this did not significantly change the observed contrast and the variation between the methods could be accounted for by the different seed values for the random number generation.

# 7. Results and discussion

For this thesis, several hundreds of individual STEM simulations were performed using the systems specified in chapter 5. These simulations were used to create a database of STEM images in different orientations and conditions. The images can be compared against experimental results and used to characterize defects. Additionally, the different orientations and configurations could assist experimentalists in finding the optimal microscope settings in regards to imaging defect structures with atomic resolution. Furthermore, the simulated cascade defects provide indications of the contrast observed from more complex defect structures.

## 7.1 $\langle 001 \rangle$ dislocation loops

Figure 7.1 shows a STEM image simulation of an interstitial $\langle 001 \rangle$ -loop with different detector angles. The contrast of the final image is highly dependent on the detector angles used. Low collection angles are more sensitive to effects caused by phonons or strain fields [60]. This can clearly be seen in the image produced with 40-60 mrad detector angles. On the other hand, the contrast for higher angles can be thought of as coming from scattered electrons, essentially excluding the signal of the transmitted beam [61]. Subsequently, the contrast of high angle images is more dependent on the atomic structure. As a result, the underlying atomistic structure is clearer in the images produced with higher detector angles. Additionally, the overall intensity is significantly smaller for the higher detector angles.

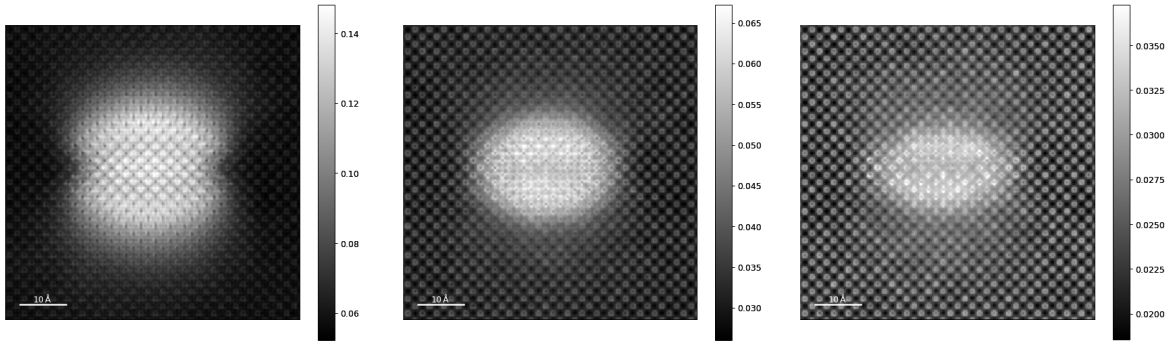


**(a)** 40-60 mrad **(b)** 60-80 mrad **(c)** 80-100 mrad

**Figure 7.1:** STEM image simulation in different detector angles of an interstitial ⟨001⟩ -loop, simulated in 100 keV with semi-angle 30 mrad. Beam direction ⟨010⟩ and defocus 0 Å.

For each simulated system a defocus series was produced. Figure 7.2 shows the full defocus series of an edge on interstitial ⟨001⟩ -loop. Different parts of the specimen are in focus with different defocus values. From the images we can see that at the extremes of the defocus range the defected region looks blurry and out of focus. With defocus value $-100$ Å the defect region shows the sharpest focus, which seems sensible as the defect is in the middle of the simulation cell that was 200 Å thick.

All the different ⟨001⟩ -loops were simulated in the microscope conditions listed in table 6.1. Figure 7.3 shows the total image intensity as a function of the detector angle for the different beam conditions. The peak of the total intensity is dependent on the probe semi-angle used. For higher semi-angles the intensity is shifted towards the higher detector angles. In addition to this, the 200 keV probe follows a similar curve to its 100 keV counterpart, but has higher overall intensity. Figure 7.4 shows the simulated images of the edge on ⟨001⟩ -loop in the different beam energies and semi-angles. The images are shown with detector angles 60-80 mrad in order to highlight the differences illustrated in figure 7.3. From the simulated images we can see that the lattice structure is more pronounced in the 200 keV beam. Furthermore, the images with larger probe semi-angles are more saturated. The difference in the image contrast is significantly smaller with 80-100 mrad detector angles for the different semi-angles at 100 keV.

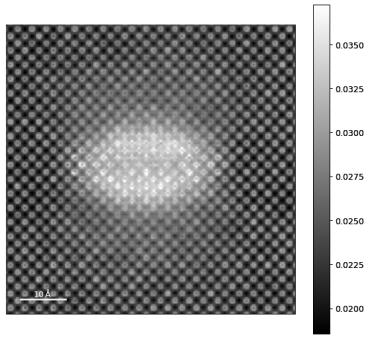


**(a)** defocus = 0 Å

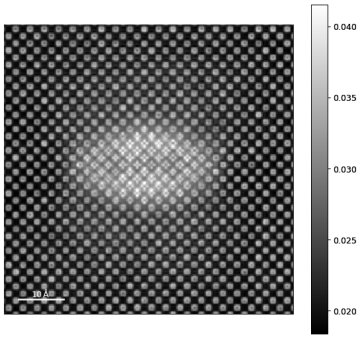


**(b)** defocus = -50 Å

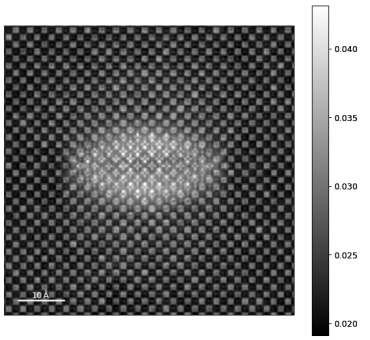


**(c)** defocus = -75 Å

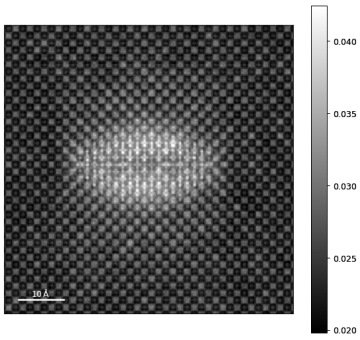


**(d)** defocus = -100 Å

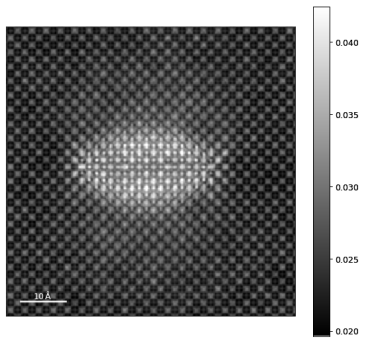


**(e)** defocus = -125 Å

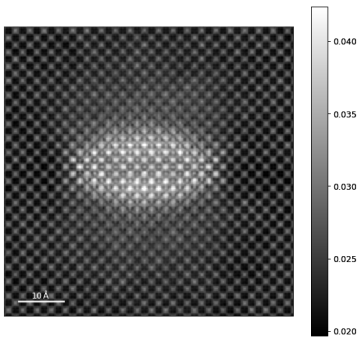


**(f)** defocus = -150 Å

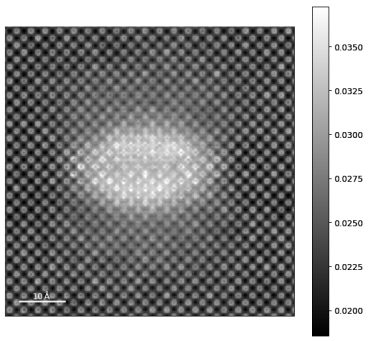


**(g)** defocus = -200 Å

**Figure 7.2:** Defocus series of an interstitial ⟨001⟩ -loop, beam direction ⟨010⟩, 100 keV, semi-angle 30 mrad with detector angle 80-100 mrad.

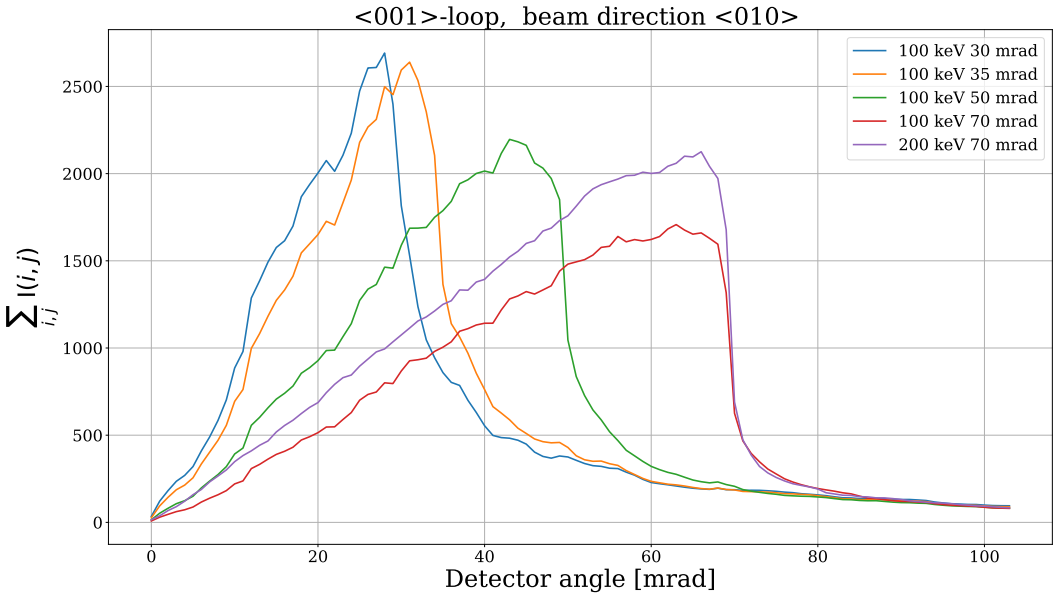


**Figure 7.3:** Total intensity as a function of detector angle for an interstitial ⟨001⟩ dislocation loop in ⟨010⟩ beam direction for different beam energies and probe semi-angles.

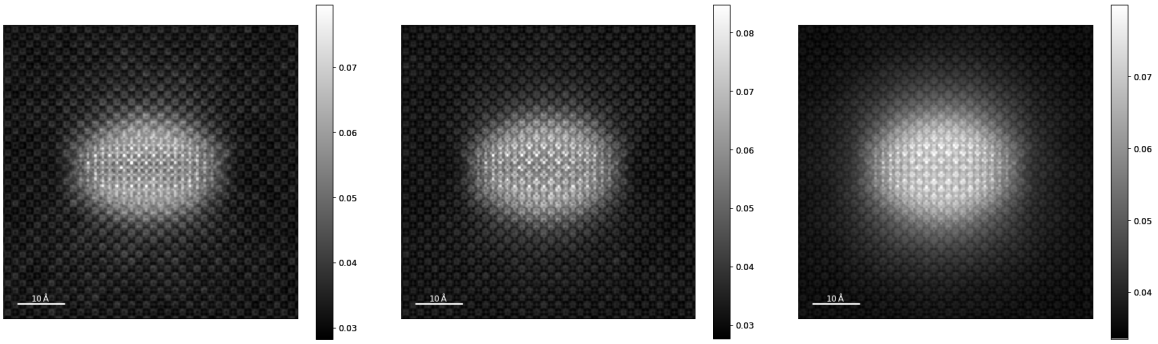

**(a)** 100 keV, 30 mrad **(b)** 100 keV, 35 mrad **(c)** 100 keV, 50 mrad

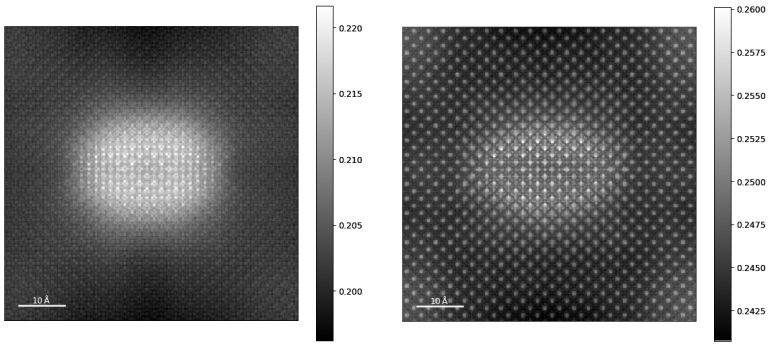

**(d)** 100 keV, 70 mrad **(e)** 200 keV, 70 mrad

**Figure 7.4:** Interstitial ⟨001⟩ -loop in beam direction ⟨010⟩ for different microscope conditions with −100 Å defocus and detector angle 60-80 mrad.

All the different beam directions for both interstitial and vacancy type ⟨001⟩ -loops are shown in figure 7.5. In the case where the dislocation is oriented parallel to the optical axis, the overall contrast of the dislocation is significantly diminished. In experimental situations where the noise in the data might be higher as well as with thicker samples, it might be hard to distinguish loops in this orientation due to insufficient contrast or the signal-to-noise ratio might be too low. Figure 7.6 shows the same systems in 40-60 mrad collection angles where the strain contrast is more discernible. The beam direction ⟨010⟩ shows differences in the strain contrast between the different loop types. The interstitial loop has a strain contrast that is bulging outwards from the center. Conversely, for the vacancy loop the strain contrast curves inwards. This difference in the strain field could be used for characterization of the loop type.

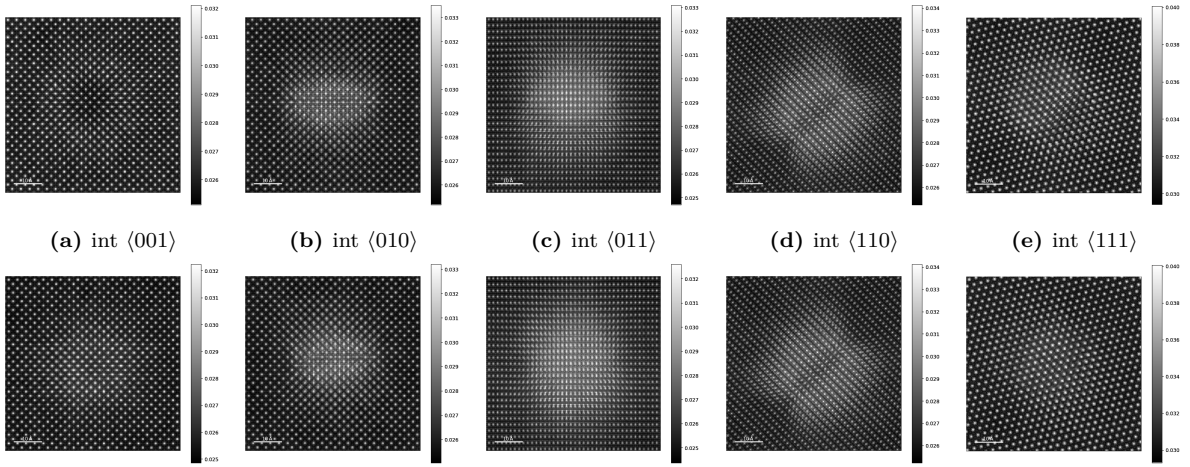

**(a)** int ⟨001⟩ **(b)** int ⟨010⟩ **(c)** int ⟨011⟩ **(d)** int ⟨110⟩ **(e)** int ⟨111⟩

**(f)** vac ⟨001⟩ **(g)** vac ⟨010⟩ **(h)** vac ⟨011⟩ **(i)** vac ⟨110⟩ **(j)** vac ⟨111⟩

**Figure 7.5:** Comparison between vacancy and interstitial ⟨001⟩ -loops in different beam directions. Images simulated with beam energy 200 keV, probe semi-angle 70 mrad, defocus −100 Å and detector angle 80-100 mrad.

Both types of ⟨001⟩ -loops in beam direction ⟨010⟩ are shown with their corresponding atomistic structures in figure 7.7. Looking at the atomistic illustration we can see perturbations in the positions of the atoms in the columns close to the dislocation, which are distinct between the two different loop types. These differences can faintly be seen from the simulated STEM images. Figure 7.8 shows the line profiles over the pixels highlighted by the yellow lines in figure 7.7. The interstitial line profile shows smaller peaks consistently on the outsides of the peaks of the atom columns. In the case of the vacancy loop, there are similar peaks on the insides of the atom columns. The difference was quantified by looking at the shape parameters of fitted skewed normal distributions for each peak separately. This was achieved by first using a rudimentary peak finding algorithm and fitting a skew normal distribution to a range of ±7 pixels for each peak. The location and the value of the shape parameter was stored for each peak. Figure 7.9 shows

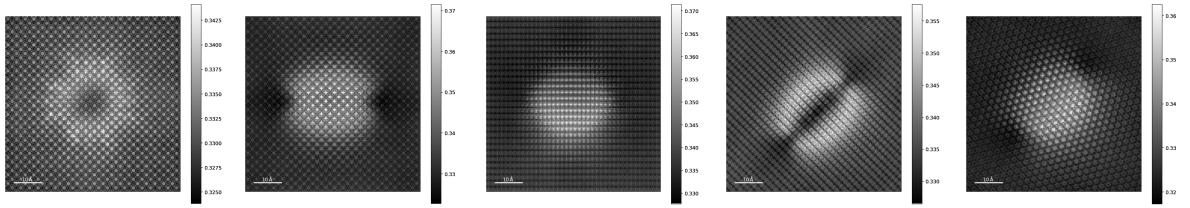

**(a)** int ⟨001⟩ **(b)** int ⟨010⟩ **(c)** int ⟨011⟩ **(d)** int ⟨110⟩ **(e)** int ⟨111⟩

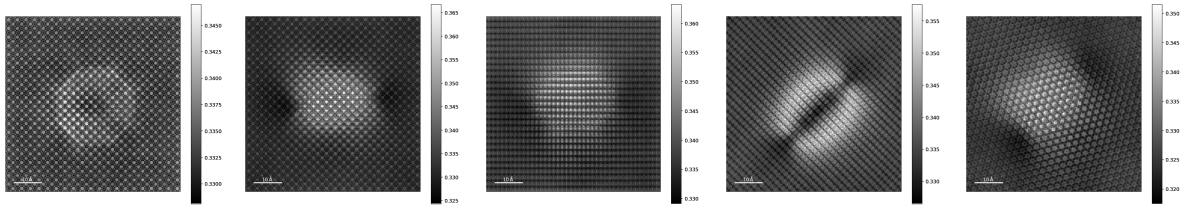

**(f)** vac ⟨001⟩ **(g)** vac ⟨010⟩ **(h)** vac ⟨011⟩ **(i)** vac ⟨110⟩ **(j)** vac ⟨111⟩

**Figure 7.6:** Comparison between vacancy and interstitial ⟨001⟩ -loops in different beam directions. Images simulated with beam energy 200 keV, probe semi-angle 70 mrad, defocus −100 Å and detector angle 40-60 mrad.

the shape parameter as a function of peak location, where we can see a clear difference between the two loop types.

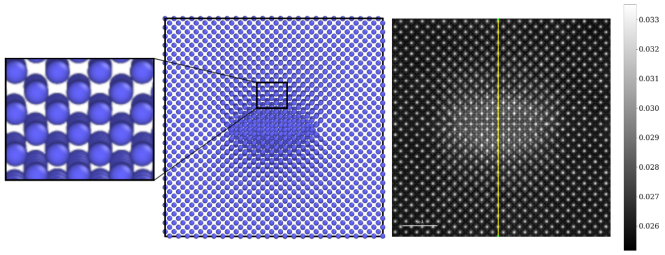

**(a)** Interstitial

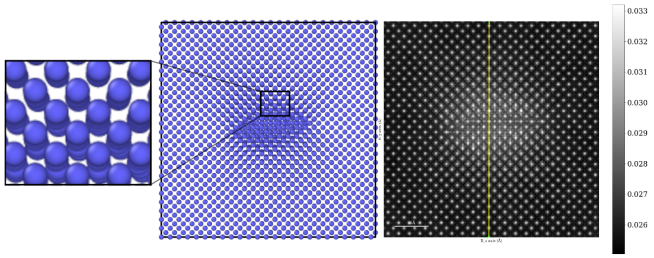

**(b)** Vacancy

**Figure 7.7:** Comparison between vacancy and interstitial ⟨001⟩ -loops in beam direction ⟨010⟩. Image simulated using 200 keV beam with semi-angle 70 mrad, defocus −100 Å and detector angle 80-100 mrad.

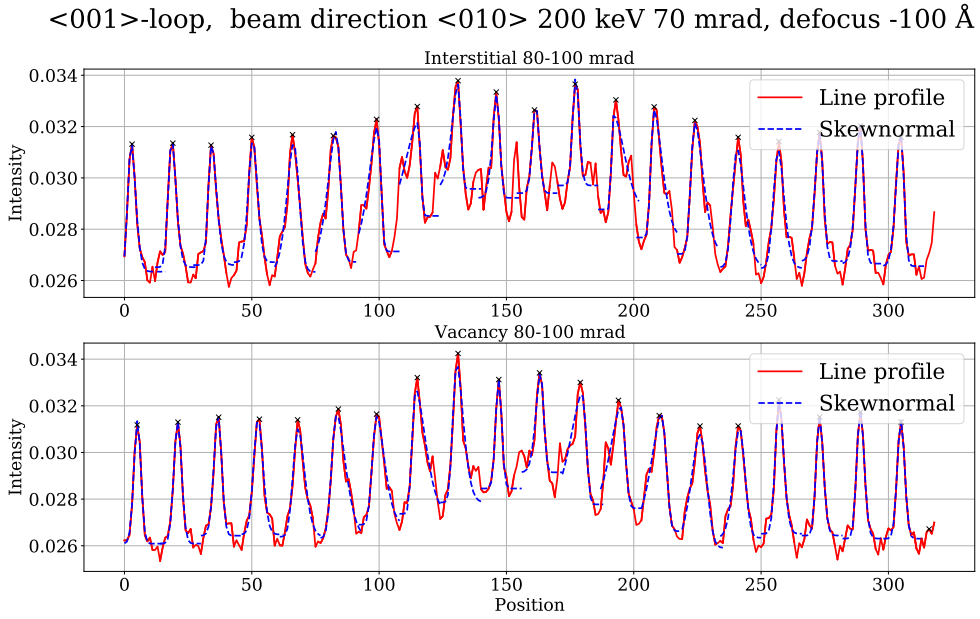


**Figure 7.8:** Line profile of interstitial and vacancy ⟨001⟩ -loop in ⟨010⟩ direction in 200 keV, probe semi-angle 70 mrad and detector angles 80-100 mrad. The x-axis is the index of the pixel along the line profile. Black crosses represent the peaks identified by the peak finding algorithm.

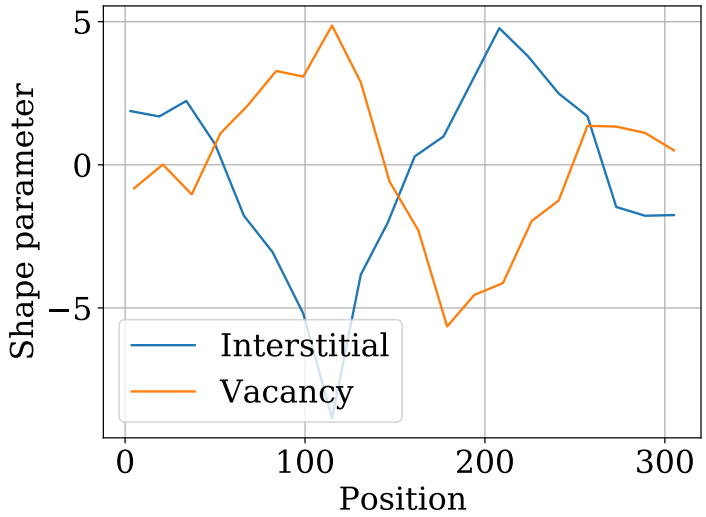


**Figure 7.9:** Value of skew normal distribution shape parameter as a function of peak position. The x-axis is the index of the pixel along the line profile.

In order to simulate spatial incoherence [62], the final images were convolved with a Gaussian function with full width half maximum (FWHM) of 0.8 Å. The convolution was performed in order to simulate the finite size of the illumination source. Figure 7.10 shows the contrast difference caused by the convolution.

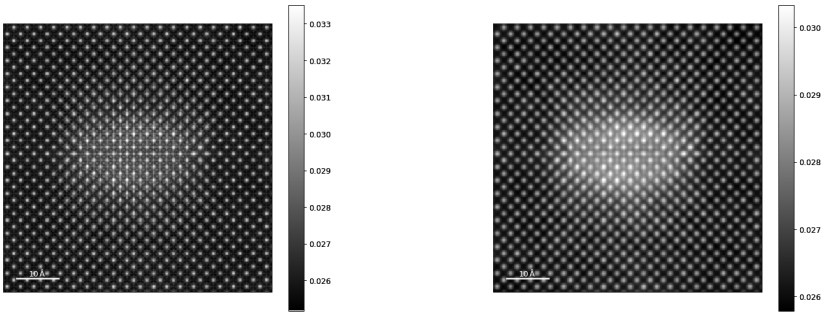

**(a)** No convolution **(b)** Convolution

**Figure 7.10:** Beam direction ⟨010⟩. Image simulated using 200 keV beam with semi-angle 70 mrad, defocus −100 Å and detector angle 80-100 mrad. Gaussian convolution was applied with 0.8 Å FWHM.

Similar line profiles as shown in figure 7.8 can be drawn for all the different defocus values and beam conditions on the convoluted images. Figure 7.11 shows the shape parameters for different defocus values. From the figures it can be seen that the difference between the interstitial and vacancy loops is dependent on the defocus used. The differences shown were only noticeable with higher detector angles (> 70 mrad) and using the 200 keV beam.

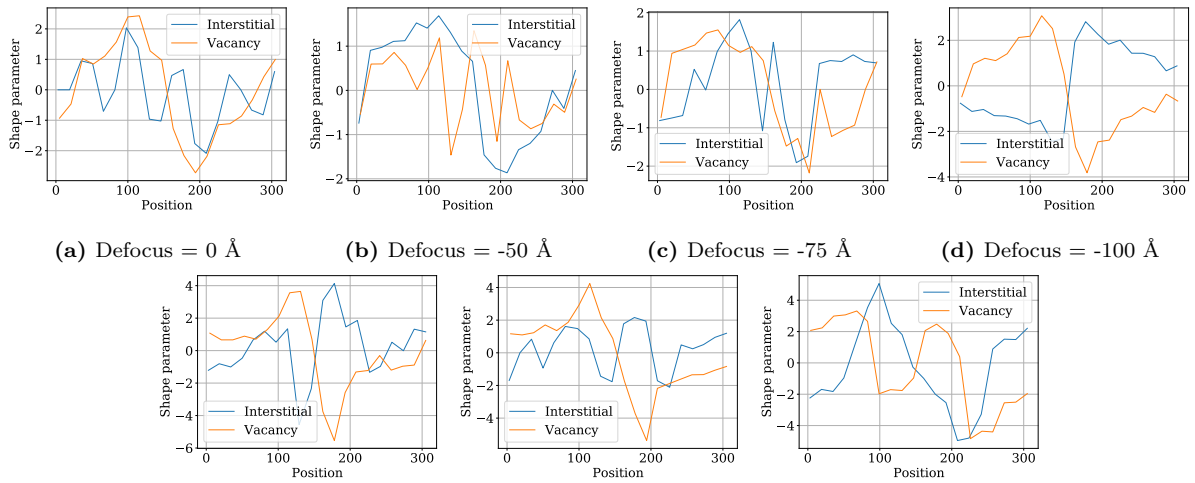


**(a)** Defocus = 0 Å **(b)** Defocus = -50 Å **(c)** Defocus = -75 Å **(d)** Defocus = -100 Å

**(e)** Defocus = -125 Å **(f)** Defocus = -150 Å **(g)** Defocus = -200 Å

**Figure 7.11:** Interstitial and vacancy ⟨001⟩ -loop in ⟨010⟩ direction in 200 keV, probe semi-angle 70 mrad and detector angles 80-100 mrad. Gaussian convolution was applied with 0.8 Å FWHM.

## 7.2 Comparison with experiment

A set of experimental images were produced by collaborators at the super STEM facility with a 100 keV Nion UltraSTEM microscope using a 35 mrad probe semi-angle. The experimental tungsten sample was imaged in the ⟨100⟩ direction. The simulated images in all the ⟨100⟩ directions were compared against the experimental results in order to identify defects from them. Figure 7.13 shows a collection of simulated ⟨001⟩ -loops with the same beam energy and semi-angle as the experimental images. Dislocations in the ⟨111⟩ direction were also simulated (not by the author) and used for comparisons. The vacancy and interstitial ⟨111⟩ -loops are shown in figure 7.14, simulated with 100 keV and 30 mrad. Using these images an edge-on ⟨001⟩ dislocation could be identified from the experimental images. Figure 7.12 shows a visual comparison between the experimental image and a simulated ⟨001⟩ dislocation loop in ⟨010⟩ beam direction. The simulated image is superimposed on top of the experimental so that the underlying lattice structure is similarly oriented and scaled.

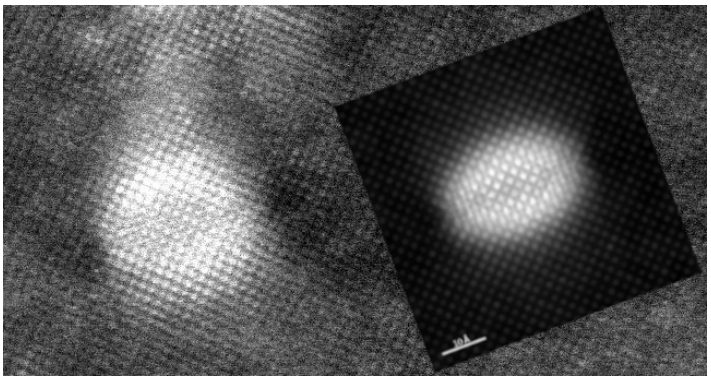

**Figure 7.12:** Comparison with experiment, 100 keV 35 mrad. Simulated image, interstitial ⟨001⟩ in ⟨010⟩ direction, 60-80 mrad detector angle in -100 Å defocus. Gaussian convolution was applied with 0.8 Å FWHM.

The experimental defect could be identified with high confidence by visually ruling out different defect types and orientations. however, the interstitial or vacancy nature of the dislocation loop could not be stated. In addition to this, it seems that the experimental dislocation is similar in size to the 3 nm diameter loop used for the simulations.

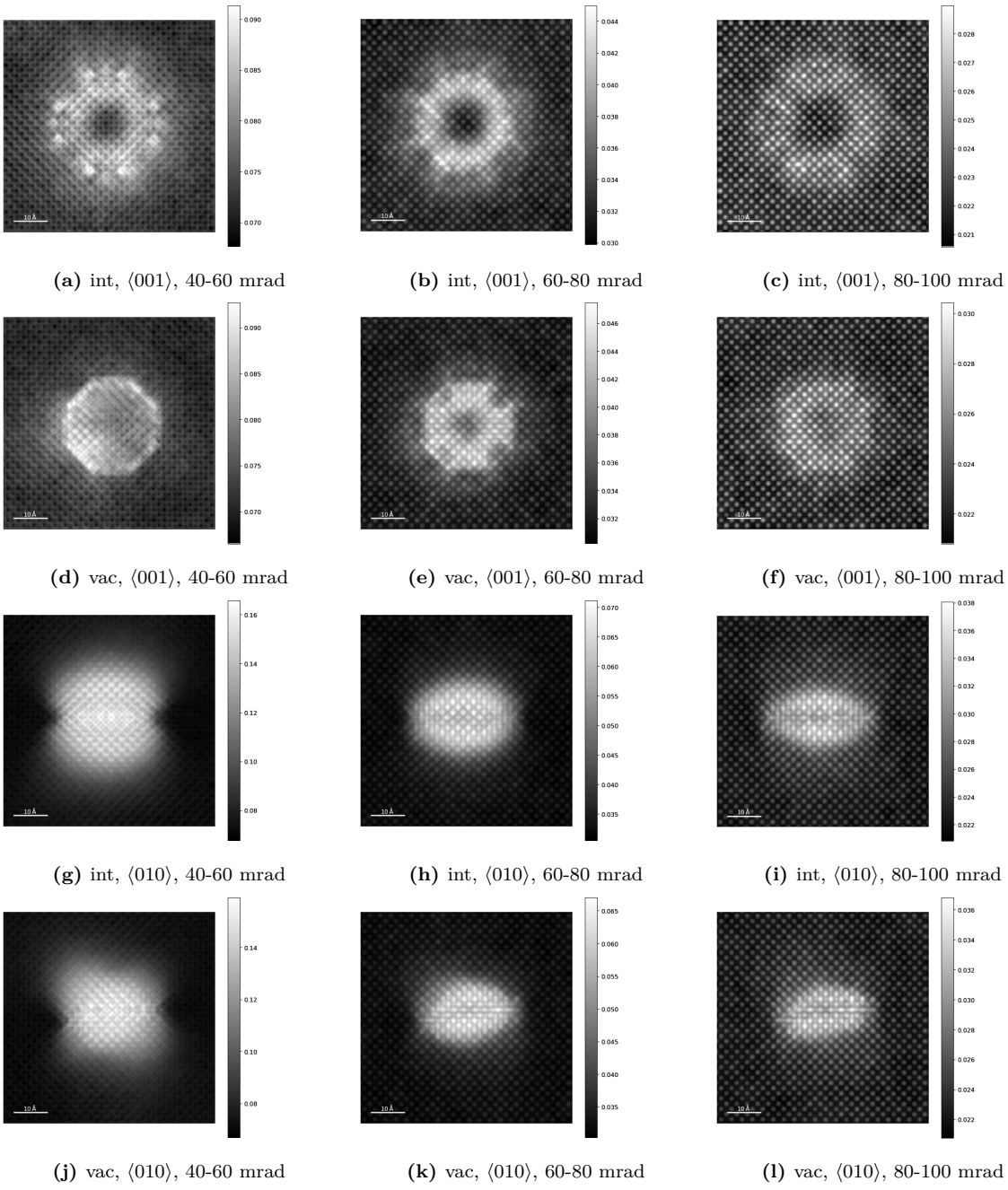

**(a)** int, ⟨001⟩, 40-60 mrad **(b)** int, ⟨001⟩, 60-80 mrad **(c)** int, ⟨001⟩, 80-100 mrad

**(d)** vac, ⟨001⟩, 40-60 mrad **(e)** vac, ⟨001⟩, 60-80 mrad **(f)** vac, ⟨001⟩, 80-100 mrad

**(g)** int, ⟨010⟩, 40-60 mrad **(h)** int, ⟨010⟩, 60-80 mrad **(i)** int, ⟨010⟩, 80-100 mrad

**(j)** vac, ⟨010⟩, 40-60 mrad **(k)** vac, ⟨010⟩, 60-80 mrad **(l)** vac, ⟨010⟩, 80-100 mrad

**Figure 7.13:** Simulated ⟨001⟩ -loops in diffrent directions and detector angles imaged in 100 keV, 35 mrad and -100 Å defocus. Gaussian convolution was applied with 0.8 Å FWHM.

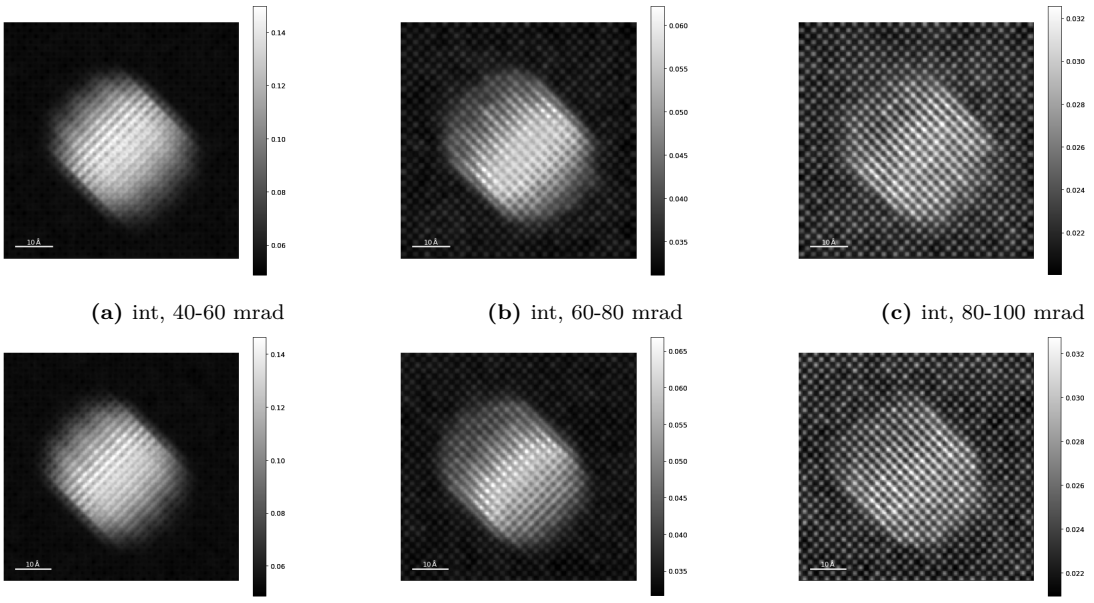

**(a)** int, 40-60 mrad **(b)** int, 60-80 mrad **(c)** int, 80-100 mrad

**(d)** vac, 40-60 mrad **(e)** vac, 60-80 mrad **(f)** vac, 80-100 mrad

**Figure 7.14:** Simulated STEM images of ⟨111⟩ -loops in beam direction ⟨100⟩ with 100 keV, semi-angle 30 mrad and defocus −100 Å. Gaussian convolution was applied with 0.8 Å FWHM.

## 7.3 Loop sizes and smaller defect clusters

Loop size determination is a major consideration in the characterization of dislocations. For smaller defects, conventional TEM diffraction contrast imaging is usually used. Methods such as two-beam imaging and weak-beam diffraction imaging are generally utilized [8]. However, accurate size determination for defects smaller than 5nm, seems to be difficult using these methods [63]. Weak-beam diffraction images can be simulated by numerical solutions of electron diffraction theory. Using simulated weak-beam diffraction images, loop sizes can be determined within about 20 % of the true loop size in the case of very small defects [9]. These simulations were performed with dislocation loops with a diameter of 2nm or higher. It is also stated that the elasticity theory approximation used might not be valid for loops smaller than this [9, 64]. The limited visibility of smaller defects in TEM [65], makes the accurate estimation of defect counts problematic.

Considering these limitations, STEM images provide an alternative method for accurate size determination for very small defects. Liu *et al.* [10] reports that number density estimations in TEM are reliable for clusters larger than 1nm. Additionally, they conclude that STEM methods should be used for number density estimations for smaller defect clusters, due to TEMs visibility limit. Figures 7.15 show STEM image simulations of ⟨001⟩ -loops of different sizes. These loops were created in similar fashion as the other dislocations. The resolution provided by STEM allows for direct observation of far smaller defects in comparison to the weak-beam simulation methods, allowing for distinguishing

of sub-nanometer defect clusters. Simulations like these could be used for size determination of dislocation loops and smaller defect clusters. A line profile drawn through a 1nm diameter loop with different detector angles can be seen in figure 7.16. The figure shows that the different detector angles do not significantly change the observed size of the defect.

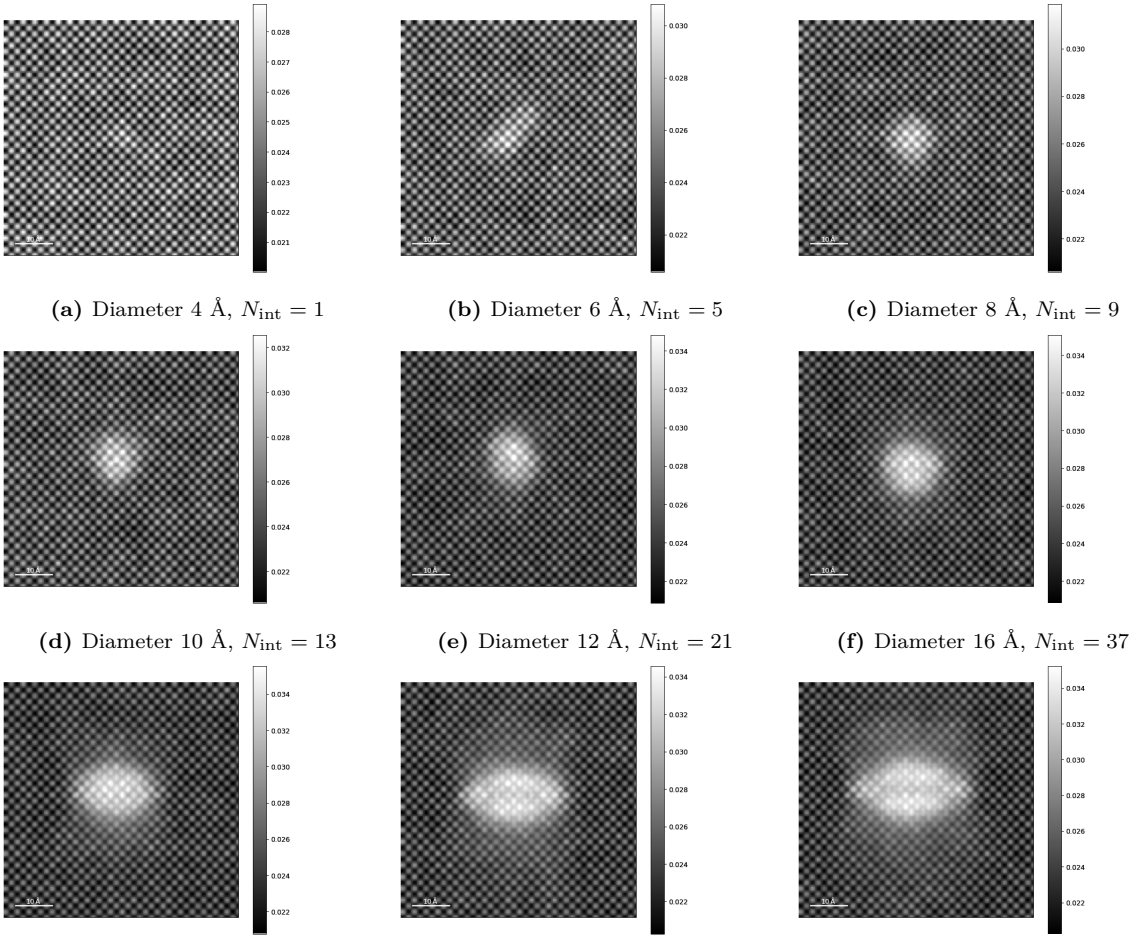

**(a)** Diameter 4 Å, $N_{\text{int}} = 1$ **(b)** Diameter 6 Å, $N_{\text{int}} = 5$ **(c)** Diameter 8 Å, $N_{\text{int}} = 9$

**(d)** Diameter 10 Å, $N_{\text{int}} = 13$ **(e)** Diameter 12 Å, $N_{\text{int}} = 21$ **(f)** Diameter 16 Å, $N_{\text{int}} = 37$

**(g)** Diameter 20 Å, $N_{\text{int}} = 61$ **(h)** Diameter 24 Å, $N_{\text{int}} = 89$ **(i)** Diameter 28 Å, $N_{\text{int}} = 121$

**Figure 7.15:** Interstitial dislocations of different sizes imaged in 100 keV, semi-angle 30 mrad, probe defocus 0 Å and detector angles 80-100 mrad. Gaussian convolution was applied to the simulated images with 0.8 Å FWHM.

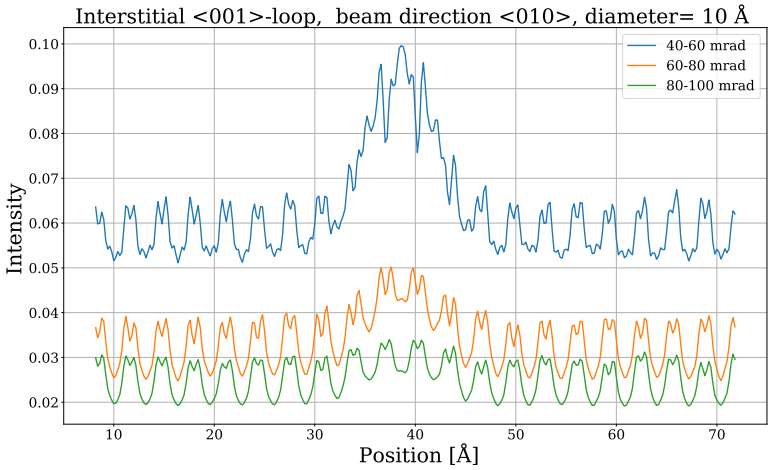


**Figure 7.16:** Line profile of 1nm diameter interstitial ⟨001⟩ -loop in 100 keV, semi-angle 30 mrad and defocus 0 Å in different detector angles.

## 7.4 Cascade defects

The smaller systems containing cascade damage from section 5.2 were simulated using a 100 keV beam energy and probe semi-angle 50 mrad. Figure 7.17 shows both the atomistic view of the defect and the corresponding simulated image. As stated before, the scanning window was chosen to cut out a small buffer region from the edges of the images. Unfortunately in this case, some point defects fall into regions which are not visible in the final image.

Individual interstitial atoms are able to create visible contrast in the images. The strain contrast from these interstitials is oriented along the ⟨111⟩ lattice directions, which is the energetically most favorable lattice direction for interstitial orientation in tungsten [66]. Single vacancies on the other hand are not visible, but voids show visible contrast. Figure 7.18 shows the cascade systems in different detector angles. The characterization of images becomes very precarious in cases where vacancy clusters, dislocations and interstitials are all in close vicinity or overlapping. Voids for example might smear the strain contrast of dislocation loops, making characterization of the dislocation very difficult.

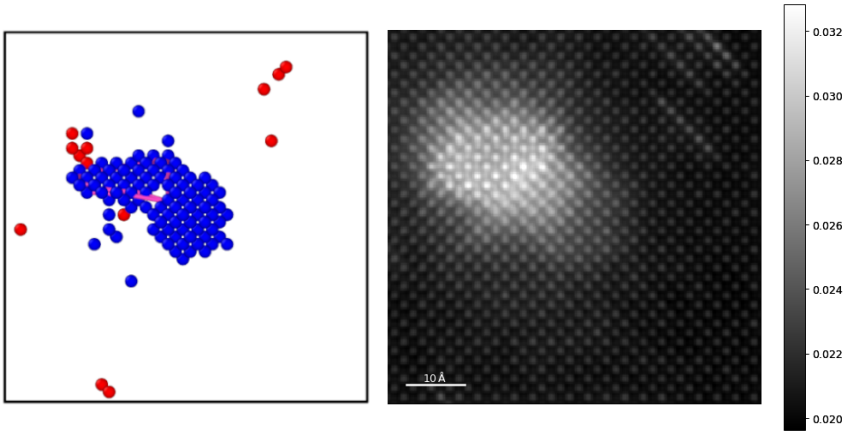


**(a)**

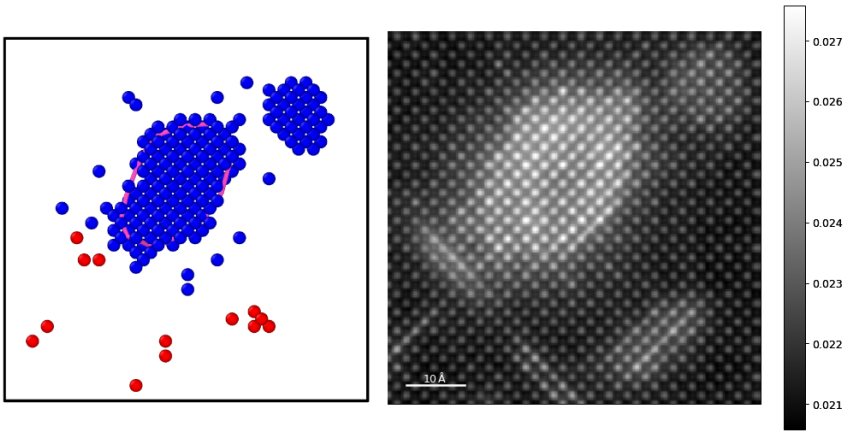


**(b)**

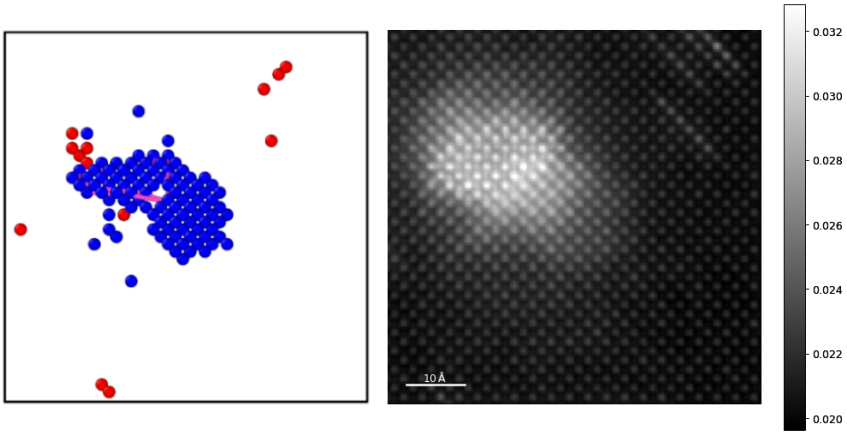


**(c)**

**Figure 7.17:** STEM image simulations of 30 keV cascade overlapping with vacancy voids. Beam energy 100 keV and semi-angle 50 mrad. STEM images are using detector angle 80-100 mrad and defocus -100 Å. Gaussian convolution was applied to the simulated images with 0.8 Å FWHM. Blue spheres are vacancies, red spheres are interstitials and the magenta lines represent dislocations in ⟨100⟩ directions.

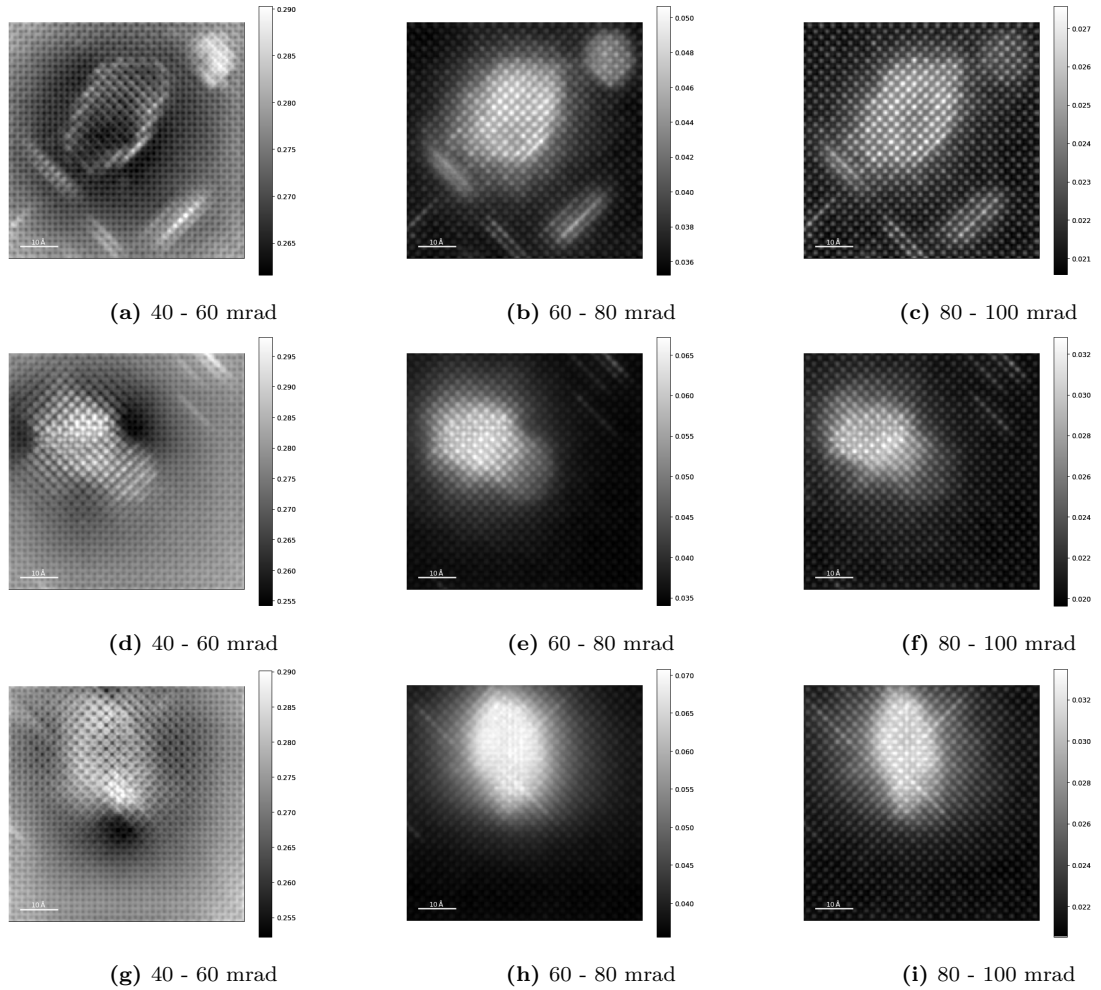

**(a)** 40 - 60 mrad **(b)** 60 - 80 mrad **(c)** 80 - 100 mrad

**(d)** 40 - 60 mrad **(e)** 60 - 80 mrad **(f)** 80 - 100 mrad

**(g)** 40 - 60 mrad **(h)** 60 - 80 mrad **(i)** 80 - 100 mrad

**Figure 7.18:** 30 keV cascade damage in 100 keV beam energy and semi-angle 50 mrad with different detector angles in -100 Å defocus. Gaussian convolution was applied with 0.8 Å FWHM.

Figure 7.19 show the simulated STEM image of the larger cascade systems with illustrations of the underlying defect structure. These systems were simulated in 100 keV and semi-angle 35 mrad. The simulated STEM images show the averaged intensity from 30 different frozen phonon configurations. For each different orientation a defocus series was performed. Figure 7.20 shows a defocus series of one of the simulated orientations. By comparing the simulated images to the experimental example in figure 7.21, we can observe that the contrast of the defects in the simulated images have similar characteristics compared to the experimental example. Further research is needed in order to demonstrate that simulated images like these could be used to infer properties of more complex defect structures from experimental images.

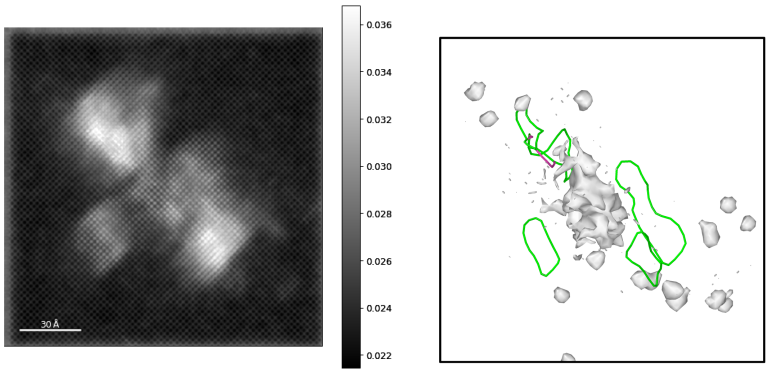


**(a)** beam direction ⟨001⟩

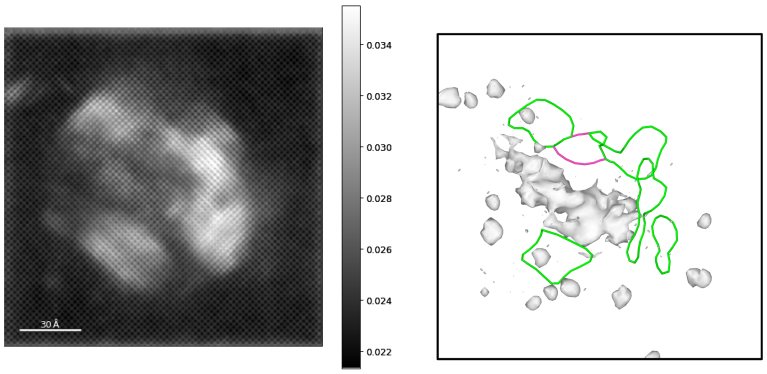


**(b)** beam direction ⟨010⟩

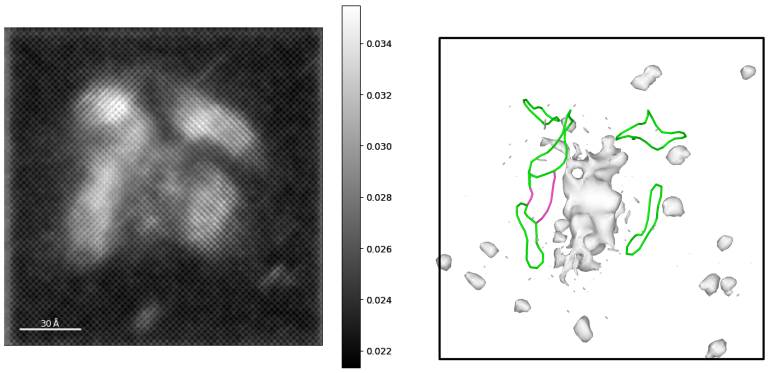


**(c)** beam direction ⟨100⟩

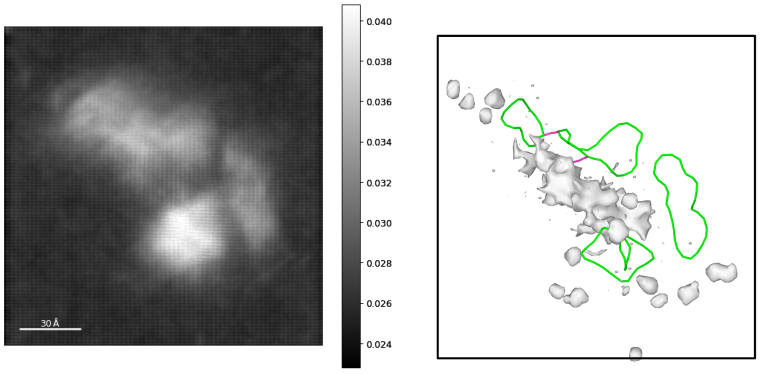


**(d)** beam direction ⟨011⟩

**Figure 7.19:** Simulated STEM image of cascade damage in 100 keV, semi-angle 35 mrad, -150 Å defocus and detector angles 80-100 mrad. Gaussian convolution was applied with 0.8 Å FWHM. On the right of the simulated images the underlying structure is visualized. Here, white regions illustrate defect structures, green lines represent dislocations in ⟨111⟩ directions and magenta lines represent dislocations in ⟨100⟩ directions.

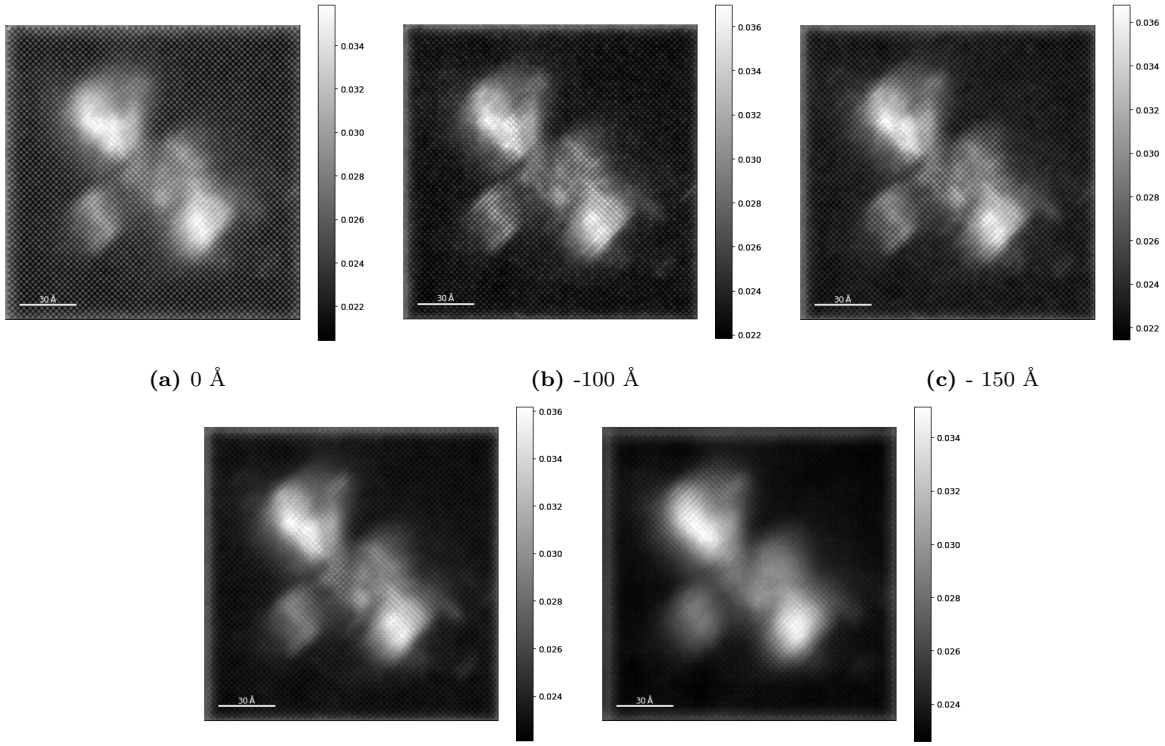


**(a)** 0 Å **(b)** -100 Å **(c)** - 150 Å

**(d)** - 200 Å **(e)** - 300 Å

**Figure 7.20:** Defocus series of simulated STEM image of cascade damage in 100 keV, semi-angle 35 mrad, beam direction ⟨001⟩ and detector angles 80-100 mrad. Gaussian convolution was applied with 0.8 Å FWHM.

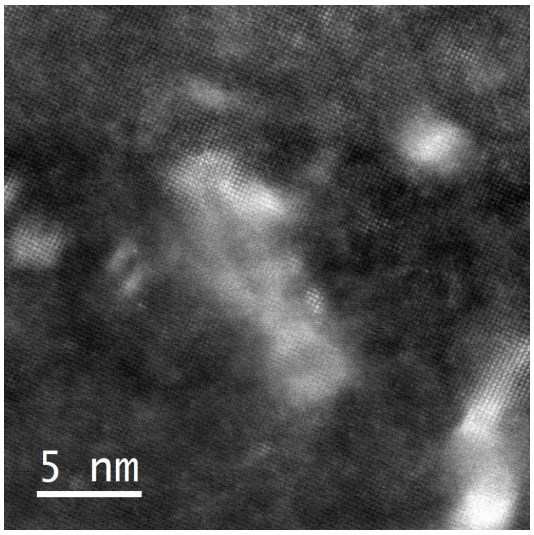


**Figure 7.21:** Experimental STEM image at 100 keV and 35 mrad. The image is from the same experimental dataset as discussed in section 7.2.

# 8. Conclusions

In this thesis, molecular dynamics simulations were used to create lattice defects in tungsten. Scanning transmission electron microscope images were simulated based on the defected systems. The STEM images were simulated using a multislice implementation. Various convergence tests were performed to validate the STEM images and optimized parameters were found.

A database of simulated STEM images of $\langle 001 \rangle$ dislocation loops was created and ultimately compared to experimental results. Defocus series of $\langle 001 \rangle$ dislocation loops were created in various beam energies and semi-angles. Our results demonstrate that the simulated images could be used in the characterization of defects from experimental data. Furthermore, it was demonstrated that sub-nanometer defects can be distinguished from STEM simulated images. Observable differences between interstitial and vacancy loops were found. These differences were dependent on the defocus and were mainly distinguishable with higher detector angles and with the 200 keV beam.

In addition to this, simulated STEM images of cascade damage from collision cascade simulations were produced. Individual interstitial atoms could be discerned from the images. Furthermore, in cases where voids were overlapping with dislocations, the defect characterization became very difficult. The larger defects produced from 150 keV collision cascades could not be simulated in a single run, due to computational constraints. In order to simulate the $16 \cdot 16 \cdot 30$ nm simulation cell each individual frozen phonon configuration had to be simulated separately. The larger system included various different dislocations and defect clusters. These images demonstrate that STEM image simulations of cascade damage are feasible. Furthermore, simulated images like these could provide valuable insight into the characterization of experimental images of radiation damage.

# 9. Acknowledgements

The simulated STEM images in this thesis were created as a part of a EUROfusion funded "Atomic Resolution Advanced Characterisation techniques for Radiation Damage study (AtomCRaD)" project. This work has been carried out within the framework of the EURO- fusion Consortium and has received funding from the Euratom research and training programme 2014–2018 and 2019–2020 under Grant Agreement No. 633053. The views and opinions expressed herein do not necessarily reflect those of the European Commission. Computational resources were provided by the University of Helsinki, FCGI – Finnish Grid and Cloud Infrastructure [67] and cineca HPC. Experimental STEM images were provided by Eric Prestat and ⟨111⟩ simulations were performed by Patrik Ikäheimonen.

# References


[1] W. D. Callister and D. G. Rethwisch, *Materials science and engineering: an introduction*. Wiley New York, 2018, vol. 9.

[2] J. Matolich, H. Nahm, and J. Moteff, "Swelling in neutron irradiated tungsten and tungsten-25 percent rhenium," *Scripta Metallurgica*, vol. 8, no. 7, pp. 837 – 841, 1974. [Online]. Available: http://www.sciencedirect.com/science/article/pii/0036974874903044

[3] A. Hasegawa, M. Fukuda, K. Yabuuchi, and S. Nogami, "Neutron irradiation effects on the microstructural development of tungsten and tungsten alloys," *Journal of Nuclear Materials*, vol. 471, pp. 175–183, 2016. [Online]. Available: https://www.sciencedirect.com/science/article/pii/S0022311515302932

[4] K. Ehrlich, "Materials research towards a fusion reactor," *Fusion Engineering and Design*, vol. 56-57, pp. 71 – 82, 2001. [Online]. Available: http://www.sciencedirect.com/science/article/pii/S0920379601002368

[5] R. Abernethy, "Predicting the performance of tungsten in a fusion environment: a literature review," *Materials Science and Technology*, vol. 33, no. 4, pp. 388–399, 2017.

[6] M. Rieth, S. Dudarev, S. G. de Vicente, J. Aktaa, T. Ahlgren, S. Antusch, D. Armstrong, M. Balden, N. Baluc, M.-F. Barthe, W. Basuki, M. Battabyal, C. Becquart, D. Blagoeva, H. Boldyryeva, J. Brinkmann, M. Celino, L. Ciupinski, J. Correia, A. D. Backer, C. Domain, E. Gaganidze, C. García-Rosales, J. Gibson, M. Gilbert, S. Giusepponi, B. Gludovatz, H. Greuner, K. Heinola, T. Höschen, A. Hoffmann, N. Holstein, F. Koch, W. Krauss, H. Li, S. Lindig, J. Linke, C. Linsmeier, P. López-Ruiz, H. Maier, J. Matejicek, T. Mishra, M. Muhammed, A. Muñoz, M. Muzyk, K. Nordlund, D. Nguyen-Manh, J. Opschoor, N. Ordás, T. Palacios, G. Pintsuk, R. Pippan, J. Reiser, J. Riesch, S. Roberts, L. Romaner, M. Rosiński, M. Sanchez, W. Schulmeyer, H. Traxler, A. Ureña, J. van der Laan, L. Veleva, S. Wahlberg, M. Walter, T. Weber, T. Weitkamp,

S. Wurster, M. Yar, J. You, and A. Zivelonghi, "Recent progress in research on tungsten materials for nuclear fusion applications in europe," *Journal of Nuclear Materials*, vol. 432, no. 1, pp. 482 – 500, 2013. [Online]. Available: http://www.sciencedirect.com/science/article/pii/S0022311512004278

[7] M. L. Jenkins and M. A. Kirk, *Characterisation of radiation damage by transmission electron microscopy*. CRC Press, 2000.

[8] M. Jenkins, "Characterisation of radiation-damage microstructures by tem," *Journal of Nuclear Materials*, vol. 216, pp. 124 – 156, 1994. [Online]. Available: http://www.sciencedirect.com/science/article/pii/0022311594900108

[9] Z. Zhou, M. L. Jenkins, S. L. Dudarev, A. P. Sutton, and M. A. Kirk, "Simulations of weak-beam diffraction contrast images of dislocation loops by the many-beam howie–basinski equations," *Philosophical Magazine*, vol. 86, no. 29-31, pp. 4851–4881, 2006. [Online]. Available: https://doi.org/10.1080/14786430600615041

[10] C. Liu, L. He, Y. Zhai, B. Tyburska-Püschel, P. Voyles, K. Sridharan, D. Morgan, and I. Szlufarska, "Evolution of small defect clusters in ion-irradiated 3c-sic: Combined cluster dynamics modeling and experimental study," *Acta Materialia*, vol. 125, pp. 377 – 389, 2017. [Online]. Available: http://www.sciencedirect.com/science/article/pii/S1359645416309569

[11] J. Marian, B. Wirth, R. Schäublin, J. Perlado, and T. D. de la Rubia, "< 100>-loop characterization in $\alpha$-fe: comparison between experiments and modeling," *Journal of nuclear materials*, vol. 307, pp. 871–875, 2002.

[12] W. WU and R. SCHÄUBLIN, "Synergistic effects of anisotropy and image force on tem diffraction contrast of dislocation loops," *Journal of Microscopy*, vol. 278, no. 1, pp. 29–41, 2020. [Online]. Available: https://onlinelibrary.wiley.com/doi/abs/10.1111/jmi.12884

[13] W. Wu and R. Schäublin, "Tem diffraction contrast images simulation of dislocations," *Journal of microscopy*, vol. 275, no. 1, pp. 11–23, 2019.

[14] C.-C. Chen, C. Zhu, E. R. White, C.-Y. Chiu, M. Scott, B. Regan, L. D. Marks, Y. Huang, and J. Miao, "Three-dimensional imaging of dislocations in a nanoparticle at atomic resolution," *Nature*, vol. 496, no. 7443, pp. 74–77, 2013.

[15] J. M. Johnson, S. Im, W. Windl, and J. Hwang, "Three-dimensional imaging of individual point defects using selective detection angles in annular dark field scanning transmission electron microscopy," *Ultramicroscopy*, vol. 172, pp. 17–29, 2017.

[16] P. Phillips, M. Brandes, M. Mills, and M. De Graef, "Diffraction contrast stem of dislocations: Imaging and simulations," *Ultramicroscopy*, vol. 111, no. 9-10, pp. 1483–1487, 2011.

[17] R. Pitts, S. Carpentier, F. Escourbiac, T. Hirai, V. Komarov, S. Lisgo, A. Kukushkin, A. Loarte, M. Merola, A. Sashala Naik, R. Mitteau, M. Sugihara, B. Bazylev, and P. Stangeby, "A full tungsten divertor for iter: Physics issues and design status," *Journal of Nuclear Materials*, vol. 438, pp. S48 – S56, 2013, proceedings of the 20th International Conference on Plasma-Surface Interactions in Controlled Fusion Devices. [Online]. Available: http://www.sciencedirect.com/science/article/pii/S0022311513000160

[18] S. Krat, Y. Gasparyan, A. Pisarev, I. Bykov, M. Mayer, G. de Saint Aubin, M. Balden, C. Lungu, and A. Widdowson, "Erosion at the inner wall of jet during the discharge campaign 2011–2012 in comparison with previous campaigns," *Journal of Nuclear Materials*, vol. 456, pp. 106 – 110, 2015. [Online]. Available: http://www.sciencedirect.com/science/article/pii/S0022311514005376

[19] V. Philipps, "Tungsten as material for plasma-facing components in fusion devices," *Journal of Nuclear Materials*, vol. 415, no. 1, Supplement, pp. S2 – S9, 2011, proceedings of the 19th International Conference on Plasma-Surface Interactions in Controlled Fusion. [Online]. Available: http://www.sciencedirect.com/science/article/pii/S0022311511001589

[20] L. Ciupiński, O. Ogorodnikova, T. Płociński, M. Andrzejczuk, M. Rasiński, M. Mayer, and K. Kurzydłowski, "Tem observations of radiation damage in tungsten irradiated by 20mev w ions," *Nuclear Instruments and Methods in Physics Research Section B: Beam Interactions with Materials and Atoms*, vol. 317, pp. 159 – 164, 2013, proceedings of the 19th International Workshop on Inelastic Ion-Surface Collisions (IISC-19), Frauenchiemsee, Germany, 16-21 September 2012. [Online]. Available: http://www.sciencedirect.com/science/article/pii/S0168583X13003558

[21] R. Abernethy, "Predicting the performance of tungsten in a fusion environment: a literature review," *Materials Science and Technology*, vol. 33, no. 4, pp. 388–399, 2017. [Online]. Available: https://doi.org/10.1080/02670836.2016.1185260

[22] J. Marian, C. S. Becquart, C. Domain, S. L. Dudarev, M. R. Gilbert, R. J. Kurtz, D. R. Mason, K. Nordlund, A. E. Sand, L. L. Snead *et al.*, "Recent advances in modeling and simulation of the exposure and response of tungsten to fusion energy conditions," *Nuclear Fusion*, vol. 57, no. 9, p. 092008, 2017.

[23] N. W. Ashcroft, N. D. Mermin *et al.*, "Solid state physics [by] neil w. ashcroft [and] n. david mermin." 1976.

[24] K. Nordlund, S. J. Zinkle, T. Suzudo, R. S. Averback, A. Meinander, F. Granberg, L. Malerba, R. Stoller, F. Banhart, B. Weber, F. Willaime, S. Dudarev, and D. Simeone, *Primary radiation damage in materials: Review of current understanding and proposed new standard displacement damage model to incorporate in-cascade mixing and defect production efficiency effects.* Paris, France: OECD Nuclear Energy Agency, 2015.

[25] A. Sand, J. Byggmästar, A. Zitting, and K. Nordlund, "Defect structures and statistics in overlapping cascade damage in fusion-relevant bcc metals," *Journal of Nuclear Materials*, vol. 511, pp. 64 – 74, 2018, special Section on '18th International Conference on Fusion Reactor Materials'. [Online]. Available: http://www.sciencedirect.com/science/article/pii/S0022311518305178

[26] E. Levo, F. Granberg, C. Fridlund, K. Nordlund, and F. Djurabekova, "Radiation damage buildup and dislocation evolution in equiatomic multicomponent alloys," *J. Nucl. Mater.*, vol. 490, p. 323, 2017.

[27] A. Fellman, A. E. Sand, J. Byggmästar, and K. Nordlund, "Radiation damage in tungsten from cascade overlap with voids and vacancy clusters," *Journal of Physics: Condensed Matter*, 2019. [Online]. Available: http://iopscience.iop.org/10.1088/1361-648X/ab2ea4

[28] J. Byggmästar, F. Granberg, A. Sand, A. Pirttikoski, R. Alexander, M. Marinica, and K. Nordlund, "Collision cascades overlapping with self-interstitial defect clusters in fe and w," *Journal of Physics: Condensed Matter*, vol. 31, no. 24, p. 245402, 2019.

[29] B. J. Alder and T. E. Wainwright, "Phase transition for a hard sphere system," *The Journal of chemical physics*, vol. 27, no. 5, pp. 1208–1209, 1957.

[30] M. Prutton and M. Prutton, *Introduction to surface physics.* Clarendon Press Oxford, 1994.

[31] M. Allen and D. Tildesley, *Computer Simulation of Liquids.* Oxford, England: Oxford University Press, 1989.

[32] M. S. Daw, S. M. Foiles, and M. I. Baskes, "The embedded-atom method: a review of theory and applications," *Materials Science Reports*, vol. 9, no. 7, pp. 251 – 310, 1993. [Online]. Available: http://www.sciencedirect.com/science/article/pii/092023079390001U

[33] J. Ziegler, J. Biersack, and U. Littmark, *The Stopping and Range of Ions in Matter*. New York: Pergamon, 1985.

[34] J. Tersoff, "New empirical approach for the structure and energy of covalent systems," *Physical review B*, vol. 37, no. 12, p. 6991, 1988.

[35] K. Nordlund, 2010, PARCAS computer code. The main principles of the molecular dynamics algorithms are presented in [68, 69]. The adaptive time step and electronic stopping algorithms are the same as in [70].

[36] J. Ziegler, SRIM-2013 software package, available online at *http://www.srim.org*.

[37] H. J. Berendsen, J. v. Postma, W. F. van Gunsteren, A. DiNola, and J. Haak, "Molecular dynamics with coupling to an external bath," *The Journal of chemical physics*, vol. 81, no. 8, pp. 3684–3690, 1984.

[38] W. G. Hoover, "Canonical dynamics: Equilibrium phase-space distributions," *Physical review A*, vol. 31, no. 3, p. 1695, 1985.

[39] H. C. Andersen, "Molecular dynamics simulations at constant pressure and/or temperature," *The Journal of chemical physics*, vol. 72, no. 4, pp. 2384–2393, 1980.

[40] M. Parrinello and A. Rahman, "Polymorphic transitions in single crystals: A new molecular dynamics method," *Journal of Applied physics*, vol. 52, no. 12, pp. 7182–7190, 1981.

[41] L. De Broglie, "Recherches sur la théorie des quanta," Ph.D. dissertation, Migration-université en cours d'affectation, 1924.

[42] E. Ruska, "The development of the electron microscope and of electron microscopy," *Bioscience reports*, vol. 7, no. 8, pp. 607–629, 1987.

[43] M. Knoll and E. Ruska, "Das elektronenmikroskop," *Zeitschrift für physik*, vol. 78, no. 5-6, pp. 318–339, 1932.

[44] M. Von Ardenne, "Das elektronen-rastermikroskop," *Zeitschrift für Physik*, vol. 109, no. 9-10, pp. 553–572, 1938.

[45] R. Brydson, *Aberration-corrected analytical transmission electron microscopy*. John Wiley & Sons, 2011, vol. 3.

[46] E. J. Kirkland, *Advanced computing in electron microscopy*. Springer, 1998.

[47] O. Scherzer, "The theoretical resolution limit of the electron microscope," *Journal of Applied Physics*, vol. 20, no. 1, pp. 20–29, 1949.

[48] J. M. Cowley and A. F. Moodie, "The scattering of electrons by atoms and crystals. i. a new theoretical approach," *Acta Crystallographica*, vol. 10, no. 10, pp. 609–619, 1957.

[49] K. Ishizuka, "Fft multislice method–the silver anniversary," *Microscopy and Microanalysis*, vol. 10, no. 1, p. 34, 2004.

[50] R. F. Loane, P. Xu, and J. Silcox, "Thermal vibrations in convergent-beam electron diffraction," *Acta Crystallographica Section A: Foundations of Crystallography*, vol. 47, no. 3, pp. 267–278, 1991.

[51] A. Pryor, C. Ophus, and J. Miao, "A streaming multi-gpu implementation of image simulation algorithms for scanning transmission electron microscopy," *Advanced structural and chemical imaging*, vol. 3, no. 1, p. 15, 2017.

[52] C. Ophus, "A fast image simulation algorithm for scanning transmission electron microscopy," *Advanced structural and chemical imaging*, vol. 3, no. 1, p. 13, 2017.

[53] S. Plimpton, "Fast parallel algorithms for short-range molecular dynamics," *Journal of computational physics*, vol. 117, no. 1, pp. 1–19, 1995.

[54] G. J. Ackland and R. Thetford, "An improved n-body semi-empirical model for body-centred cubic transition metals," *Philosophical Magazine A*, vol. 56, no. 1, pp. 15–30, 1987. [Online]. Available: https://doi.org/10.1080/01418618708204464

[55] Y. Zhong, K. Nordlund, M. Ghaly, and R. S. Averback, "Defect production in tungsten: A comparison between field-ion microscopy and molecular-dynamics simulations," *Phys. Rev. B*, vol. 58, pp. 2361–2364, Aug 1998. [Online]. Available: https://link.aps.org/doi/10.1103/PhysRevB.58.2361

[56] A. Stukowski, "Visualization and analysis of atomistic simulation data with ovito-the open visualization tool," *Modelling and Simulation in Materials Science and Engineering*, vol. 18, no. 1, p. 015012, 2010. [Online]. Available: http://stacks.iop.org/0965-0393/18/i=1/a=015012

[57] A. Stukowski and K. Albe, "Extracting dislocations and non-dislocation crystal defects from atomistic simulation data," *Modelling and Simulation in Materials Science and Engineering*, vol. 18, no. 8, p. 085001, 2010. [Online]. Available: http://stacks.iop.org/0965-0393/18/i=8/a=085001

[58] A. Sand, K. Nordlund, and S. Dudarev, "Radiation damage production in massive cascades initiated by fusion neutrons in tungsten," *Journal of Nuclear Materials*, vol. 455, no. 1, pp. 207 – 211, 2014, proceedings of the 16th

International Conference on Fusion Reactor Materials (ICFRM-16). [Online]. Available: http://www.sciencedirect.com/science/article/pii/S002231151400364X

[59] E. Cosgriff and P. Nellist, "A bloch wave analysis of optical sectioning in aberration-corrected stem," *Ultramicroscopy*, vol. 107, no. 8, pp. 626 – 634, 2007. [Online]. Available: http://www.sciencedirect.com/science/article/pii/S0304399107000022

[60] D. A. Muller, N. Nakagawa, A. Ohtomo, J. L. Grazul, and H. Y. Hwang, "Atomic-scale imaging of nanoengineered oxygen vacancy profiles in srtio 3," *Nature*, vol. 430, no. 7000, pp. 657–661, 2004.

[61] S. J. Pennycook and P. D. Nellist, *Scanning transmission electron microscopy: imaging and analysis*. Springer Science & Business Media, 2011.

[62] D. O. Klenov, S. D. Findlay, L. J. Allen, and S. Stemmer, "Influence of orientation on the contrast of high-angle annular dark-field images of silicon," *Physical Review B*, vol. 76, no. 1, p. 014111, 2007.

[63] M. L. Jenkins, M. A. Kirk, and H. Fukushima, "On the application of the weak-beam technique to the determination of the sizes of small point-defect clusters in ion-irradiated copper," *Microscopy*, vol. 48, no. 4, pp. 323–332, 1999.

[64] Z. Zhou, S. Dudarev, M. Jenkins, A. Sutton, and M. Kirk, "On the atomic displacement fields of small interstitial dislocation loops," *Materials Science and Engineering: A*, vol. 400-401, pp. 80 – 83, 2005, dislocations 2004. [Online]. Available: http://www.sciencedirect.com/science/article/pii/S0921509305002625

[65] S. Das, "Recent advances in characterising irradiation damage in tungsten for fusion power," *SN Applied Sciences*, vol. 1, no. 12, p. 1614, 2019.

[66] P. M. Derlet, D. Nguyen-Manh, and S. Dudarev, "Multiscale modeling of crowdion and vacancy defects in body-centered-cubic transition metals," *Physical Review B*, vol. 76, no. 5, p. 054107, 2007.

[67] Finnish grid and cloud infrastructure, urn:nbn:fi:research-infras-2016072533.

[68] K. Nordlund, M. Ghaly, R. S. Averback, M. Caturla, T. Diaz de la Rubia, and J. Tarus, "Defect production in collision cascades in elemental semiconductors and fcc metals," *Phys. Rev. B*, vol. 57, no. 13, pp. 7556–7570, 1998.

[69] M. Ghaly, K. Nordlund, and R. S. Averback, "Molecular dynamics investigations of surface damage produced by kev self-bombardment of solids," *Phil. Mag. A*, vol. 79, no. 4, p. 795, 1999.

[70] K. Nordlund, "Molecular dynamics simulation of ion ranges in the 1 – 100 kev energy range," *Comput. Mater. Sci.*, vol. 3, p. 448, 1995.